Small-Signal Modeling and Controller Parameters Tuning of Grid-Forming VSCs With Adaptive Virtual Impedance-Based Current Limitation

Heng Wu, *Member, IEEE*, and Xiongfei Wang, *Senior Member, IEEE*

***Abstract*—The adaptive virtual impedance (VI) control emerges as an attractive solution to limit the current of grid-forming voltage-source converters (GFM-VSCs) during grid faults. Yet, the adaptive VI-based current limitation relies on the detection of the current magnitude, which introduces nonlinear dynamics that challenges the controller parameters tuning of GFM-VSCs. This article develops the small-signal model of GFM-VSCs with adaptive VI-based current limitation, from which, the dynamic impact of the adaptive VI is explicitly revealed. Considering such impact, a holistic controller parameters tuning method for GFM-VSC is proposed to guarantee the small-signal stability of the system. Simulation and experimental tests are performed to verify the effectiveness of the theoretical analysis and the proposed parameters tuning method.**

***Index Terms*—Current limitation, grid-forming (GFM), small-signal model, virtual impedance (VI), voltage-source converters (VSCs).**

I. Introduction

THE grid-forming (GFM) control is recently emerging as an attractive approach for stabilizing the power system with high penetration of voltage-source converters (VSCs) [1]. Being controlled as a voltage source behind an impedance, the operation of GFM-VSC does not rely on a stiff voltage source in the ac grid, and hence, it can operate stably in an ultra-weak grid, where the short-circuit ratio approaches 0 [1]. This is one of main benefits of GFM-VSCs compared with the grid-following (GFL)-VSCs [2]–[4].

While the voltage-source behavior of GFM-VSCs helps to stabilize the power system, it poses additional challenges to the current limitation of VSC during grid faults. Differing from synchronous generators with 6–8 per unit (p.u.) overcurrent capability, the current of GFM-VSC should be limited within 1.5–2 p.u. during grid faults [5]. Hence, the overcurrent limitation is one of the key design considerations for GFM-VSCs [6]–[8].

A straightforward approach for current limitation is to switch GFM-VSC to the GFL control during grid faults, where the fault current can be controlled with a dedicated current loop with proper current reference settings [2], [9], [10]. In recent years, many research efforts can be found in this direction to improve the current limit dynamics as well as transient stability of GFM-VSC [9]–[11]. While the state-of-the-art solution can guarantee the satisfactory performance of GFM-VSC itself during the fault-ride through (FRT), it does not change the fundamental nature that GFM-VSC is controlled as a current source, rather than a voltage source, during grid faults, which might limit the potential benefits of GFM-VSCs to the power system during the fault period [8], [12]. As demonstrated by simulation studies from National Grid ESO [13], the voltage source behavior of GFM-VSC enables an almost instantaneous (<5 ms) reactive current injection when it is subjecting to grid faults, which is beneficial for boosting the grid voltage and facilitates the fault recovery [8], [12], [13]. Yet, this benefit is diminished if GFM-VSC is switched to the GFL control during grid faults, with which, the orientation of the injected current relies on the grid synchronization, and a much slower (>30 ms) dynamics of reactive current injection is yielded [8], [12], [13]. Hence, there is an increasing demand for operating GFM-VSC as a voltage source during grid faults, which can be found in recent technical report from European Network of Transmission System Operators for Electricity [14] and the draft grid code from National grid ESO [15]. To that end, the current limitation needs to be realized by directly limiting the output voltage of VSC, rather than switching to the GFL control [16].

The virtual impedance (VI) control is commonly used to limit the current of GFM-VSC while retaining its voltage source behavior during grid faults, with which, the fault current would introduce a fictitious voltage drop across the VI such that the terminal voltage of VSC is naturally reduced [17]. Yet, the design of VI is nontrivial since it requires the prior knowledge of fault conditions, which is often impossible in practice [18]. Hence, the adaptive VI is recently introduced to overcome the design challenge of the fixed VI [6], [19]–[21]. The basic idea of adaptive VI is to adjust the value of VI based on the fault current magnitude, such that the current limitation can be automatically realized without any prior knowledge of fault conditions.

There have been increasing research efforts made on the adaptive VI-based current limitation, such as its dynamic performance enhancement [6], and clarifying its impact on the critical

Manuscript received July 26, 2021; revised November 2, 2021; accepted December 7, 2021. Date of publication December 15, 2021; date of current version February 18, 2022. Recommended for publication by Associate Editor M. S. ElMoursi. *(Corresponding author: Xiongfei Wang.)*

The authors are with AAU Energy, Aalborg University, 9220 Aalborg, Denmark (e-mail: hew@energy.aau.dk; xwa@energy.aau.dk).

Color versions of one or more figures in this article are available at https://doi.org/10.1109/TPEL.2021.3135693.

Digital Object Identifier 10.1109/TPEL.2021.3135693

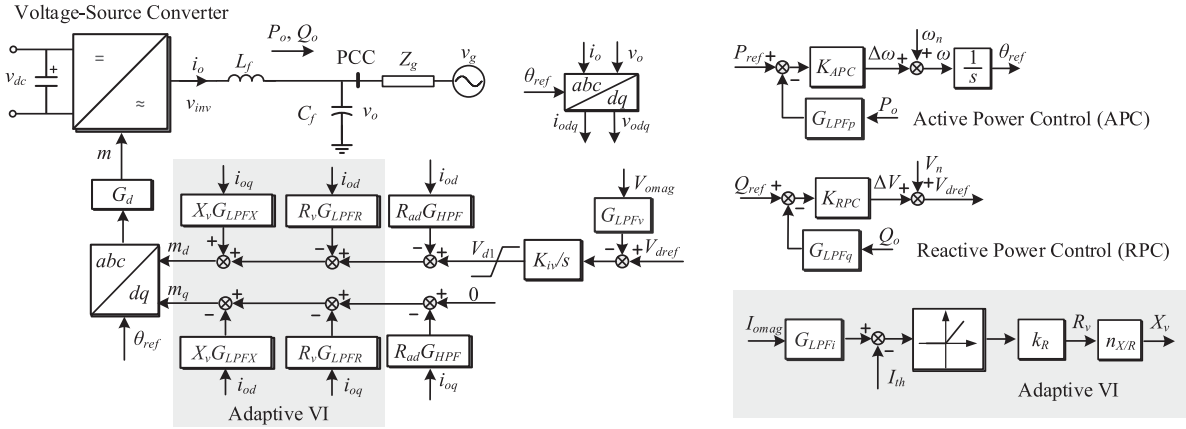

Fig. 1. GFM-VSC with the SLVM control and adaptive VI-based current limitation.

clearing time and the post-fault synchronization dynamics of GFM-VSCs [19], [20]. However, in those works, the parameters tuning of adaptive VI only considers the static fault current limitation requirement, from which, only the proportional gain of adaptive VI can be analytically derived [21]. The selection of cutoff frequencies of low-pass filters (LPFs) used in adaptive VI, which is critical to system's small-signal stability, is often made by trial and error. On the other hand, the parameters tuning of power control loops of GFM-VSC often considers its normal operation without using the adaptive VI [22]–[27]. Hence, the small-signal stability of power control loops with the adaptive VI activated remains unclear.

It is, therefore, important to develop a holistic modeling and controller parameters tuning method for GFM-VSCs with the adaptive VI. However, the adaptive VI control modifies the value of VI based on the detected current magnitude, which is essentially nonlinear and involves frequency-coupling dynamics, as will be revealed later in this article. To the best knowledge of authors, only a few attempts are recently reported to understand the small-signal stability of GFM-VSC with adaptive VI [21]. Yet, only the numerical, rather than the analytical small-signal model, is derived in [21], which offers limited insight on the controller parameters tuning.

To fill this void, this article develops an analytical small-signal model of GFM-VSC with the adaptive VI. It is, for the first time, revealed that the nonlinearity of the adaptive VI control would introduce the frequency coupling dynamics into GFM-VSCs, which is found to be crucial to the stability of the system. On this basis, a holistic parameters tuning method for different control loops of GFM-VSC is proposed to guarantee the small-signal stability of the system. Finally, experimental tests are performed to corroborate the theoretical analysis and the proposed parameters tuning approach.

II. Adaptive VI-Based Current Limitation

A. System Description

Fig. 1 shows the single-line diagram of a three-phase GFM-VSC with adaptive VI-based current limitation. Instead of using dual loop vector-voltage control, the single-loop voltage magnitude (SLVM) control is adopted in this article due to its superior small-signal stability [25], [28]. The GFM-VSC is connected to the point of common coupling (PCC) through an LC filter, and Z_g represents the grid impedance. P_o/Q_o and v_o/i_o denote the output active/reactive power and output voltage/current of VSC, while $v_{\rm inv}$ and v_g are the inverter bridge voltage and grid voltage, respectively. The GFM-VSC synchronizes with the power grid through the active power control (APC), where the active power-frequency (P–ω) droop control is used [7], which is given by

$$\theta_{\rm ref} = \frac{1}{s}\left[\omega_n + K_{\rm APC}\left(P_{\rm ref} - G_{{\rm LPF}p}P_o\right)\right] \tag{1}$$

where $\theta_{\rm ref}$ is the angle reference that is used for dq transformation. ω_n represents the nominal angular frequency. $K_{\rm APC}$ is the P–ω droop coefficient. $G_{{\rm LPF}\,p} = \omega_p/(s+\omega_p)$ represents the first-order LPF used for the active power measurement with the cutoff frequency ω_p.

On the other hand, the voltage magnitude reference of GFM-VSC is regulated by the reactive power control (RPC), e.g., the reactive power–voltage (Q–V) droop control that is given by [7]

$$V_{d{\rm ref}} = V_n + K_{\rm RPC}\left(Q_{\rm ref} - G_{{\rm LPF}q}Q_o\right) \tag{2}$$

where $V_{d{\rm ref}}$ is the voltage magnitude reference, while V_n is the nominal voltage magnitude. $K_{\rm RPC}$ is the Q–V droop coefficient. $G_{{\rm LPF}\,q} = \omega_q/(s+\omega_q)$ represents the first-order LPF used for the reactive power measurement with the cutoff frequency ω_q.

The SLVM control uses an integrator K_{iv}/s to regulate the magnitude of output voltage of VSC ($V_{o{\rm mag}} = \sqrt{v_{od}^2 + v_{oq}^2}$) to follow $V_{d{\rm ref}}$ [25], [28], and the first-order LPF $G_{LPFv} = \omega_{LPFv}/(s+\omega_{LPFv})$ with its cutoff frequency $\omega_{{\rm LPF}\,v}$ is adopted to filter out high-frequency noise in $V_{o{\rm mag}}$. The active damping resistor $R_{\rm ad}$ is added at the output of the K_{iv}/s to damp the synchronous resonance introduced by the power control [2]. It is worth mentioning that $R_{\rm ad}$ is usually cascaded with a high-pass filter $G_{\rm HPF} = s/(s+\omega_{\rm HPF})$ to eliminate its impact on the steady-state power control performance of GFM-VSC [2], and $\omega_{\rm HPF}$ represents the cutoff frequency of $G_{\rm HPF}$.

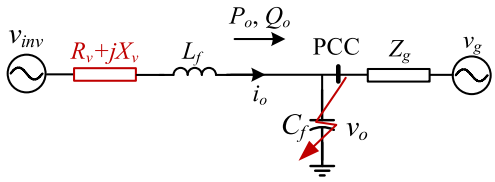

Fig. 2. Equivalent circuit of GFM-VSC under grid faults where adaptive VI is activated.

The adaptive VI is used to limit the current of GFM-VSC during grid faults, as shown in Fig. 1. X_v and R_v represent the adaptive virtual reactor and resistor, respectively, and they are given by [19]–[21]

$$R_v = \begin{cases} k_R\left(G_{\mathrm{LPF}i} I_{\mathrm{omag}} - I_{th}\right), & \text{if } \mathrm{I_{omag}} \geq \mathrm{I_{th}} \\ 0, & \text{if } I_{\mathrm{omag}} < I_{\mathrm{th}} \end{cases}$$
$$X_v = n_{X/R} R_v \tag{3}$$

where $I_{o\mathrm{mag}}$ represents the magnitude of output current of VSC and I_{th} is the threshold current beyond which the adaptive VI will be activated. k_R is the proportional gain of adaptive virtual resistor and $n_{X/R}$ represents the *X*/*R* ratio of adaptive VI. It is also noted from Fig. 1 that LPFs are used for $I_{o\mathrm{mag}}$ measurement (i.e., $G_{\mathrm{LPF}i}$) and implementation of X_v and R_v (i.e., $G_{\mathrm{LPF}X}$ and $G_{\mathrm{LPF}R}$), and their transfer functions are given by

$$G_{\mathrm{LPF}R}(s) = \frac{\omega_{\mathrm{LPF}R}}{s + \omega_{\mathrm{LPF}R}} \tag{4.1}$$
$$G_{\mathrm{LPF}X}(s) = \frac{\omega_{\mathrm{LPF}X}}{s + \omega_{\mathrm{LPF}X}} \tag{4.2}$$
$$G_{\mathrm{LPF}i}(s) = \frac{\omega_{\mathrm{LPF}i}}{s + \omega_{\mathrm{LPF}i}} \tag{4.3}$$

where $\omega_{\mathrm{LPF}R}$, $\omega_{\mathrm{LPF}X}$, and $\omega_{\mathrm{LPF}i}$ represent the cutoff frequencies of $G_{\mathrm{LPF}R}$, $G_{\mathrm{LPF}X}$, and $G_{\mathrm{LPF}i}$, respectively. These LPFs have crucial impacts on system's small-signal stability and will be detailed in Sections III and IV.

In the end, the modulation signals in *dq* frame (m_d and m_q) will be transformed to *abc* frame through *dq*/*abc* transformation in order to generate three-phase switching signals for VSC [7]. G_d(s) represents the transfer function of the time delay, i.e., $\mathrm{G}_d(\mathrm{s}) = \mathrm{e}^{-sTd}$, where T_d is the time delay [29].

B. Tuning of Adaptive VI Based on Static Current Limit Requirement

Fig. 2 illustrates the equivalent circuit of GFM-VSC under grid faults where adaptive VI is activated. It is known from (3) that there are two parameters, i.e., $n_{X/R}$ and k_R, to be determined for implementing the adaptive VI. Generally, $n_{X/R}$>3 is required to guarantee the inductive behavior of adaptive VI [19]–[21], and $n_{X/R} = 5$ is selected in this article. On the other hand, k_R should be tuned to enable GFM-VSC of limiting its fault current within its current rating (I_{lim}) under the worst case, i.e., the three-phase bolted fault at PCC [19]–[21]. In that case, the PCC voltage approximates to zero and there are around 1 p.u. voltage being imposed on the adaptive VI and L_f, and the

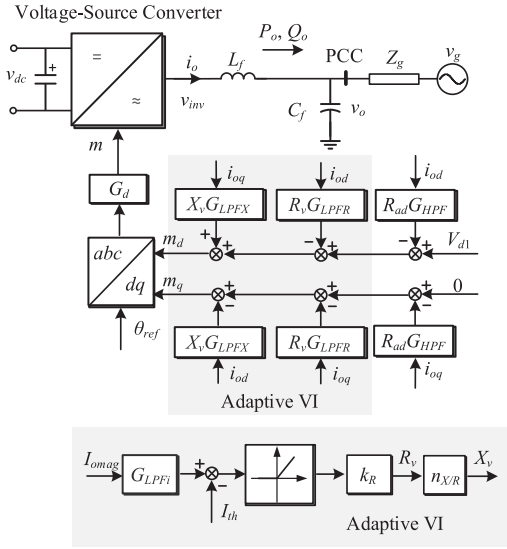

Fig. 3. GFM-VSC with adaptive VI only.

magnitude of the static fault current can be calculated as

$$I_{o\mathrm{mag}} = \frac{V_n}{\sqrt{R_v^2 + \left(X_v + X_f\right)^2}} \leq I_{\mathrm{lim}}. \tag{5}$$

Substituting (3) into (5), the minimum value of k_R that guaranteeing the static current limit performance can be calculated as

$$k_R \geq k_{R\_\min} = \frac{-n_{X/R}X_f + \sqrt{\left(n_{X/R}^2 + 1\right)\frac{V_n^2}{I_{\mathrm{lim}}^2} - X_f^2}}{\left(n_{X/R}^2 + 1\right)\left(I_{\mathrm{lim}} - I_{th}\right)}. \tag{6}$$

III. Small-Signal Modeling of Adaptive VI Loop

The GFM control given by Fig. 1 exhibits a typical cascaded control architecture, where the APC/RPC loops and the SLVM control loop can be treated as outer loops due to their low control bandwidth [25], whereas the adaptive VI control is served as the inner loop. Following the standard design philosophy of the cascaded control system that requires stabilizing the inner loop first [30], this section and Section IV will perform the small-signal modeling and parameters tuning of GFM-VSC by considering the adaptive VI only, as shown in Fig. 3. The dynamics of outer loops will be temporarily ignored but will be reconsidered in Section V, and the impact of adaptive VI on the parameters tuning of outer loops will also be addressed therein.

For clarity, the steady-state values of state variables are represented by capital letter with subscript 0, e.g., $I_{o\mathrm{mag}0}$ represents the magnitude of steady-state output current of VSC. On the other hand, the small-signal representations of state variables are denoted with symbol "^," e.g., $\hat{i}_{o\mathrm{mag}}$ represents the magnitude of output current of VSC under small-signal perturbation.

The magnitude of VSC's output current is calculated as [20]

$$I_{o\mathrm{mag}} = \sqrt{i_{od}^2 + i_{oq}^2}. \tag{7}$$

Linearizing (7) around the operating point $i_{od} = I_{od0}$, $i_{oq} = I_{oq0}$, which yields

$$\begin{aligned}\hat{i}_{\text{omag}} &= \left.\frac{\partial I_{\text{omag}}}{\partial i_{od}}\right|_{i_{od}=I_{od0}} \cdot \hat{i}_{od} + \left.\frac{\partial I_{\text{omag}}}{\partial i_{oq}}\right|_{i_{oq}=I_{oq0}} \cdot \hat{i}_{oq} \\ &= \frac{I_{od0}\hat{i}_{od}+I_{oq0}\hat{i}_{oq}}{\sqrt{I_{od0}^2+I_{oq0}^2}} = \frac{I_{od0}}{I_{\text{omag0}}}\hat{i}_{od} + \frac{I_{oq0}}{I_{\text{omag0}}}\hat{i}_{oq}.\end{aligned} \tag{8}$$

The small-signal representation of R_v and X_v can be calculated based on (3) and (8), which is given by (note that I_{th} is a constant value and thus is omitted in the small-signal analysis)

$$\begin{aligned}&\hat{R}_v = k_R G_{\text{LPF}i}\hat{i}_{\text{omag}} = k_R G_{\text{LPF}i}\left(\frac{I_{od0}}{I_{\text{omag0}}}\hat{i}_{od} + \frac{I_{oq0}}{I_{\text{omag0}}}\hat{i}_{oq}\right) \\ &\hat{X}_v = n_{X/R}\hat{R}_v.\end{aligned} \tag{9}$$

It is known from Fig. 3 that the dynamics of modulation signals in dq frame (m_d and m_q) can be expressed as

$$\begin{aligned}\begin{bmatrix} m_d \\ m_q \end{bmatrix} = &\begin{bmatrix} V_{d1} \\ 0 \end{bmatrix} - G_{\text{HPF}}\begin{bmatrix} R_{ad} & 0 \\ 0 & R_{ad} \end{bmatrix}\begin{bmatrix} i_{od} \\ i_{oq} \end{bmatrix} \\ &- \left\{ G_{\text{LPF}R}\begin{bmatrix} R_v & 0 \\ 0 & R_v \end{bmatrix} + G_{\text{LPF}X}\begin{bmatrix} 0 & -X_v \\ X_v & 0 \end{bmatrix} \right\} \\ &\begin{bmatrix} i_{od} \\ i_{oq} \end{bmatrix}.\end{aligned} \tag{10}$$

It is worth noting that R_v and X_v in (10) are also state variables. Therefore, the small-signal representation of (10) can be expressed as

$$\begin{aligned}\begin{bmatrix} \hat{m}_d \\ \hat{m}_q \end{bmatrix} = &\begin{bmatrix} \hat{v}_{d1} \\ 0 \end{bmatrix} - G_{\text{HPF}}\begin{bmatrix} R_{ad} & 0 \\ 0 & R_{ad} \end{bmatrix}\begin{bmatrix} \hat{i}_{od} \\ \hat{i}_{oq} \end{bmatrix} \\ &- G_{\text{LPF}R}\begin{bmatrix} R_{v0}\hat{i}_{od} + I_{od0}\hat{R}_v & 0 \\ 0 & R_{v0}\hat{i}_{oq} + I_{oq0}\hat{R}_v \end{bmatrix} \\ &- G_{\text{LPF}X}\begin{bmatrix} 0 & -X_{v0}\hat{i}_{oq} - I_{oq0}\hat{X}_v \\ X_{v0}\hat{i}_{od} + I_{od0}\hat{X}_v & 0 \end{bmatrix}.\end{aligned} \tag{11}$$

Substituting (9) into (11), which yields

$$\begin{aligned}\begin{bmatrix} \hat{m}_d \\ \hat{m}_q \end{bmatrix} = &\begin{bmatrix} \hat{v}_{d1} \\ 0 \end{bmatrix} - G_{\text{HPF}}\begin{bmatrix} R_{ad} & 0 \\ 0 & R_{ad} \end{bmatrix}\begin{bmatrix} \hat{i}_{od} \\ \hat{i}_{oq} \end{bmatrix} \\ &- G_{\text{LPF}R}\begin{bmatrix} R_{vdd} & R_{vdq} \\ R_{vqd} & R_{vqq} \end{bmatrix}\begin{bmatrix} \hat{i}_{od} \\ \hat{i}_{oq} \end{bmatrix} \\ &- G_{\text{LPF}X}\begin{bmatrix} -X_{vqd} & -X_{vqq} \\ X_{vdd} & X_{vdq} \end{bmatrix}\begin{bmatrix} \hat{i}_{od} \\ \hat{i}_{oq} \end{bmatrix}\end{aligned} \tag{12}$$

where

$$R_{vdd} = R_{v0} + G_{\text{LPF}i}k_R\frac{I_{od0}^2}{I_{\text{omag0}}} \tag{13.1}$$

$$R_{vqq} = R_{v0} + G_{\text{LPF}i}k_R\frac{I_{oq0}^2}{I_{\text{omag0}}} \tag{13.2}$$

$$R_{vdq} = R_{vqd} = G_{\text{LPF}i}k_R\frac{I_{od0}I_{oq0}}{I_{\text{omag0}}} \tag{13.3}$$

$$X_{vdd} = n_{X/R}R_{vdd} \tag{13.4}$$

$$X_{vqq} = n_{X/R}R_{vqq} \tag{13.5}$$

$$X_{vdq} = X_{vqd} = n_{X/R}R_{vdq} = n_{X/R}R_{vqd}. \tag{13.6}$$

Define $\mathbf{Z}_{\boldsymbol{v\_tot\,dq}}$ as the total VI matrix in dq frame, i.e.,

$$\begin{aligned}\mathbf{Z}_{\mathbf{v\_totdq}} = &G_{\text{HPF}}\begin{bmatrix} R_{ad} & 0 \\ 0 & R_{ad} \end{bmatrix} + G_{\text{LPF}R}\begin{bmatrix} R_{vdd} & R_{vdq} \\ R_{vqd} & R_{vqq} \end{bmatrix} \\ &+ G_{\text{LPF}X}\begin{bmatrix} -X_{vqd} & -X_{vqq} \\ X_{vdd} & X_{vdq} \end{bmatrix}.\end{aligned} \tag{14}$$

Then, (12) can be rewritten as

$$\begin{bmatrix} \hat{m}_d \\ \hat{m}_q \end{bmatrix} = \begin{bmatrix} \hat{v}_{d1} \\ 0 \end{bmatrix} - \mathbf{Z}_{\mathbf{v\_totdq}}\begin{bmatrix} \hat{i}_{od} \\ \hat{i}_{oq} \end{bmatrix}. \tag{15}$$

It can be clearly observed from (13) and (14) that $\mathbf{Z}_{\boldsymbol{v\_tot\,dq}}$ is asymmetric, i.e., $\mathbf{Z}_{\boldsymbol{v\_tot\,dq}}(1,1) \neq \mathbf{Z}_{\boldsymbol{v\_tot\,dq}}(2,2)$, and $\mathbf{Z}_{\boldsymbol{v\_tot\,dq}}(1,2) \neq -\mathbf{Z}_{\boldsymbol{v\_tot\,dq}}(2,1)$ [31]–[34]. This asymmetry originates from the adaptive VI that is dependent on the dynamics of current magnitude $\hat{i}_{\text{omag}}$. As shown in (8), the dynamics of $\hat{i}_{\text{omag}}$ is contributed by both $\hat{i}_{od}$ and $\hat{i}_{oq}$, which leads to the inherent coupling between d- and q-axis, and ends up with an asymmetric $\mathbf{Z}_{\boldsymbol{v\_tot\,dq}}$.

Equation (15) can be further transformed to the complex-vector representation by using the following transformation matrix [31]–[34]:

$$\begin{bmatrix} x_{dq} \\ x_{dq}^* \end{bmatrix} = \underbrace{\begin{bmatrix} 1 & j \\ 1 & -j \end{bmatrix}}_{\mathbf{T}}\begin{bmatrix} x_d \\ x_q \end{bmatrix}. \tag{16}$$

Substituting (16) into (15), which yields

$$\begin{aligned}&\begin{bmatrix} \hat{m}_d \\ \hat{m}_q \end{bmatrix} = \begin{bmatrix} \hat{v}_{d1} \\ 0 \end{bmatrix} - \mathbf{Z}_{\mathbf{v\_totdq}}\begin{bmatrix} \hat{i}_{od} \\ \hat{i}_{oq} \end{bmatrix} \Leftrightarrow \\ &\mathbf{T}^{-1}\begin{bmatrix} \hat{m}_{dq} \\ \hat{m}_{dq}^* \end{bmatrix} = \begin{bmatrix} \hat{v}_{d1} \\ 0 \end{bmatrix} - \mathbf{Z}_{\mathbf{v\_totdq}}\mathbf{T}^{-1}\begin{bmatrix} \hat{i}_{odq} \\ \hat{i}_{odq}^* \end{bmatrix} \Leftrightarrow \\ &\begin{bmatrix} \hat{m}_{dq} \\ \hat{m}_{dq}^* \end{bmatrix} = \begin{bmatrix} \hat{v}_{d1} \\ \hat{v}_{d1} \end{bmatrix} - \underbrace{\mathbf{T}\mathbf{Z}_{\mathbf{v\_totdq}}\mathbf{T}^{-1}}_{\mathbf{Z}_{\mathbf{v\_totdqc}}}\begin{bmatrix} \hat{i}_{odq} \\ \hat{i}_{odq}^* \end{bmatrix}\end{aligned} \tag{17}$$

where

$$\begin{aligned}\mathbf{Z}_{\mathbf{v\_totdqc}}(1,1) = &G_{\text{HPF}}(s)R_{ad} \\ &+ G_{\text{LPF}R}(s)\left[R_{v0} + G_{\text{LPF}i}(s)\frac{k_R I_{\text{mag0}}}{2}\right] \\ &+ jn_{X/R}G_{\text{LPF}X}(s)\left[R_{v0} + G_{\text{LPF}i}(s)\frac{k_R I_{\text{mag0}}}{2}\right]\end{aligned} \tag{18.1}$$

$$\begin{aligned}\mathbf{Z}_{\mathbf{v\_totdqc}}(1,2) = &k_R G_{\text{LPF}i}(s)\left[G_{\text{LPF}R}(s)\frac{I_{od0}^2 - I_{oq0}^2}{2I_{\text{mag0}}}\right. \\ &\left.- n_{X/R}G_{\text{LPF}X}(s)\frac{I_{od0}I_{oq0}}{I_{\text{omag0}}}\right] \\ &+ jk_R G_{\text{LPF}i}(s)\left[G_{\text{LPF}R}(s)\frac{I_{od0}I_{oq0}}{I_{\text{omag0}}}\right. \\ &\left.+ n_{X/R}G_{\text{LPF}X}(s)\frac{I_{od0}^2 - I_{oq0}^2}{2I_{\text{mag0}}}\right]\end{aligned} \tag{18.2}$$

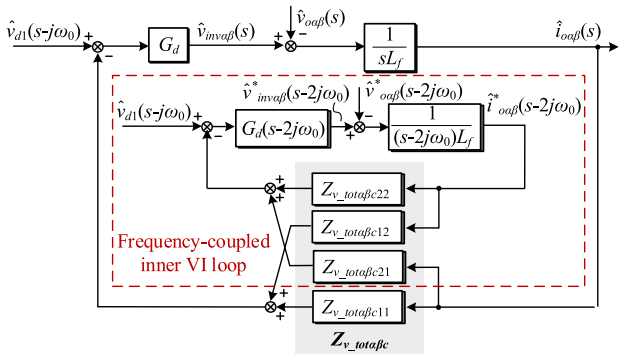

Fig. 4. Block diagram of GFM-VSC with adaptive VI only.

$$\mathbf{Z}_{\mathbf{v\_tot dqc}}(2,1) = \mathbf{Z}_{\mathbf{v\_tot dqc}}(1,2)^* \tag{18.3}$$

$$\mathbf{Z}_{\mathbf{v\_tot dqc}}(2,2) = \mathbf{Z}_{\mathbf{v\_tot dqc}}(1,1)^*. \tag{18.4}$$

It can be clearly observed from (18.2) and (18.3) that off-diagonal elements of $\boldsymbol{Z_{v\_tot\,dqc}}$ is nonzero due to the asymmetry in $\boldsymbol{Z_{v\_tot\,dq}}$ [31]–[34].

Equation (17) can be further transformed to $\alpha\beta$ frame through the frequency translation [31]–[32], which is given by

$$\begin{bmatrix} \hat{m}_{\alpha\beta}(s) \\ \hat{m}^*_{\alpha\beta}(s-2j\omega_0) \end{bmatrix} = \begin{bmatrix} \hat{v}_{d1}(s-j\omega_0) \\ \hat{v}_{d1}(s-j\omega_0) \end{bmatrix} - \mathbf{Z}_{\mathbf{v\_tot}\alpha\beta\mathbf{c}}(s) \begin{bmatrix} \hat{i}_{o\alpha\beta}(s) \\ \hat{i}^*_{o\alpha\beta}(s-2j\omega_0) \end{bmatrix} \tag{19}$$

where

$$\mathbf{Z}_{\mathbf{v\_tot}\alpha\beta\mathbf{c}}(s) = \mathbf{Z}_{\mathbf{v\_tot dqc}}(s-j\omega_0). \tag{20}$$

Equation (19) represents the small-signal model of the adaptive VI loop in $\alpha\beta$ frame, where the frequency coupling dynamics can be clearly observed from nonzero off-diagonal elements of $\boldsymbol{Z_{v\_tot\alpha\beta c}}$.

The circuit dynamics of VSC is given by [it is also expressed in a multifrequency form to make it compatible with (19)]

$$\begin{bmatrix} \hat{i}_{o\alpha\beta}(s) \\ \hat{i}^*_{o\alpha\beta}(s-2j\omega_0) \end{bmatrix} = \begin{bmatrix} \frac{\hat{v}_{\mathrm{inv}\alpha\beta}(s)-\hat{v}_{o\alpha\beta}(s)}{sL_f} \\ \frac{\hat{v}^*_{\mathrm{inv}\alpha\beta}(s-2j\omega_0)-\hat{v}^*_{o\alpha\beta}(s-2j\omega_0)}{(s-2j\omega_0)L_f} \end{bmatrix} \tag{21}$$

where

$$\begin{bmatrix} \hat{v}_{\mathrm{inv}\alpha\beta}(s) \\ \hat{v}^*_{\mathrm{inv}\alpha\beta}(s-2j\omega_0) \end{bmatrix} = \begin{bmatrix} G_d(s)\,\hat{m}_{\alpha\beta}(s) \\ G_d(s-2j\omega_0)\,\hat{m}^*_{\alpha\beta}(s-2j\omega_0) \end{bmatrix}. \tag{22}$$

Equations (19)–(22) depict the complete small-signal model of GFM-VSC by considering the impact of adaptive VI only, whose block diagram is given in Fig. 4. It can be seen from Fig. 4 that additional inner loop is introduced by frequency coupling terms, which is defined as frequency-coupled inner VI (FCIVI) loop in this article. This FCIVI loop has not been reported in previous work, yet it turns out to be crucial for the stability of the system, which will be detailed in Section IV.

IV. Parameters Tuning of Adaptive VI Loop

A. Stabilizing FCIVI Loop

In order to guarantee the stability of the adaptive VI loop, the FCIVI loop should be stabilized first. Fig. 5(a) shows the FCIVI loop that is extracted from Fig. 4, which can be further redrawn as a more familiar form shown in Fig. 5(b). Based on Fig. 5(b), the closed-loop transfer function of the FCIVI loop can be expressed as

$$\begin{aligned} Z_{\mathrm{serieseq}}(s) &= \frac{\hat{v}_{z\_\mathrm{coup}}(s)}{\hat{i}_{o\alpha\beta}(s)} \\ &= Z_{v\_tot\alpha\beta c12}(s)\, Z_{v\_tot\alpha\beta c21}(s)\, H_{\mathrm{coup}}(s) \end{aligned} \tag{23}$$

where

$$H_{\mathrm{coup}}(s) = \frac{-G_d(s-2j\omega_0)}{G_d(s-2j\omega_0)\, Z_{v\_tot\alpha\beta c22}(s) + (s-2j\omega_0)\, L_f}. \tag{24}$$

The stability of the FCIVI loop requires no right-half plan (RHP) poles in $Z_{\mathrm{serieseq}}(s)$. It is known from (18) and (20) that $Z_{v\_tot\alpha\beta c12}(s)$ and $Z_{v\_tot\alpha\beta c21}(s)$ are formed by proportional gains (R_{v0}, k_R, $n_{X/R}$, etc.) and LPFs, which do not have RHP poles. Therefore, $Z_{\mathrm{serieseq}}(s)$ will be stable provided there are no RHP poles in $H_{\mathrm{coup}}(s)$, i.e., the open-loop gain of $H_{\mathrm{coup}}(s)$ satisfies the Nyquist stability criterion [30]. It is known from Fig. 5(b) that the open-loop gain of $H_{\mathrm{coup}}(s)$ is expressed as

$$T_{\mathrm{coup}}(s) = \frac{G_d(s-2j\omega_0)\, Z_{v\_tot\alpha\beta c22}(s)}{(s-2j\omega_0)\, L_f}. \tag{25}$$

1) Without LPFs: The analysis starts with the simplest case by assuming all LPFs ($G_{\mathrm{LPF}\,i}$, $G_{\mathrm{LPF}\,X}$, and $G_{\mathrm{LPF}\,R}$) in Fig. 3 are not used. In this case, $Z_{v\_tot\alpha\beta c22}(s)$ can be calculated based on (18) and (20), which is given by

$$\begin{aligned} Z_{v\_tot\alpha\beta c22}(s) = G_{\mathrm{HPF}}(s-j\omega_0)\, R_{ad} + \left(R_{v0} + \frac{k_R I_{\mathrm{mag0}}}{2}\right) \\ - jn_{X/R}\left(R_{v0} + \frac{k_R I_{\mathrm{mag0}}}{2}\right). \end{aligned} \tag{26}$$

It is known from (25) that $T_{\mathrm{coup}}(s)$ is composed by three terms: $Z_{v\_tot\alpha\beta c22}(s)$, $1/(s-2j\omega_0)L_f$, and $G_d(s-2j\omega_0)$. The term $Z_{v\_tot\alpha\beta c22}(s)$ would introduce approximate $-90°$ phase shift due to the large imaginary part introduced by $n_{X/R}$ [see (26), R_{ad} is usually selected around 0.1 p.u. for the active damping [2], while during faults when $I_{\mathrm{mag0}} = I_{\mathrm{lim}}$, $(R_{v0} + k_R I_{\mathrm{mag0}}/2)$ and $n_{X/R}(R_{v0} + k_R I_{\mathrm{mag0}}/2)$ is calculated as 0.33 and 1.66 p.u., respectively]. On the other hand, $1/(s-2j\omega_0)L_f$ would introduce another $-90°$ phase shift in the frequency range $\omega > 2\omega_0$. By further considering the phase lag caused by the time delay term $G_d(s-2j\omega_0)$. The phase angle of $T_{\mathrm{coup}}(s)$ would inevitably crossover $-180°$ in the frequency range beyond $2\omega_0$, and the FCIVI loop will become unstable if the magnitude of $T_{\mathrm{coup}}(s)$ is higher than 1 at this $-180°$ crossover frequency. Based on parameters given in Table I, Fig. 6 shows the bode diagram of $T_{\mathrm{coup}}(s)$ without using LPFs, where a negative gain margin (GM

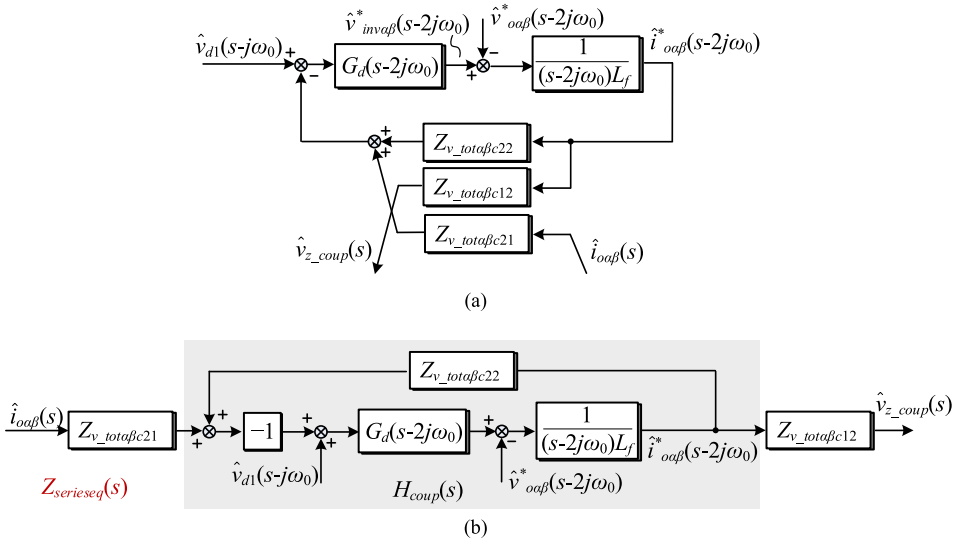

Fig. 5. (a) FCIVI loop in Fig. 4. (b) Equivalent representation of the FCIVI loop.

TABLE I
SYSTEM PARAMETERS

SYMBOL	DESCRIPTION	VALUE
V_{PCC}	PCC voltage (RMS value)	110 V
P	Power rating of the VSC	3 kW
f_g	Grid frequency	50 Hz
L_f	Filter inductance	3 mH.
C_f	Filter capacitance	50 μF
L_g	Grid inductance	2 mH
f_{sw}	Switching frequency	10 kHz
T_s	Sampling (control) period	100 μs
T_d	Time delay in the control loop	$1.5T_s$

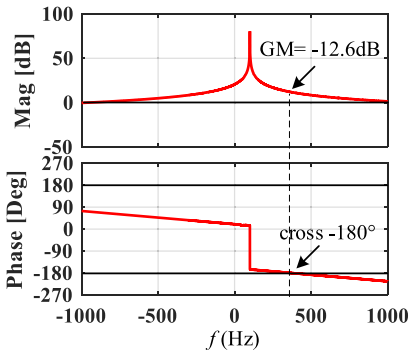

Fig. 6. Bode diagram of $T_{\rm coup}(s)$ without using LPFs, unstable.

$= -12.6$ dB) can be clearly observed. The analysis in this part highlights the risk of instability of the FCIVI loop provided LPFs are not used when implementing the adaptive VI.

2) With LPFs: By considering LPFs $G_{\rm LPF}i$, $G_{\rm LPF}X$, and $G_{\rm LPF}R$, $Z_{v\_tot\alpha\beta c22}$ can be calculated based on (18) and (20), which yields

$$Z_{v\_tot\alpha\beta c22}(s) = G_{\rm HPF}(s-j\omega_0)R_{\rm ad} + G_{\rm LPF}R(s-j\omega_0)\left[R_{v0} + G_{\rm LPF}i(s-j\omega_0)\frac{k_R I_{\rm mag0}}{2}\right] - jn_{X/R}G_{\rm LPF}X(s-j\omega_0)\left[R_{v0} + G_{\rm LPF}i(s-j\omega_0)\frac{k_R I_{\rm mag0}}{2}\right]. \quad (27)$$

The impact of those LPFs on $Z_{v\_tot\alpha\beta c22}$ as well as the stability of the FCIVI loop are analyzed as follows.

1) $G_{\rm LPF}X$: It is known from (27) that $G_{\rm LPF}X$ can reduce the magnitude of the imaginary part of $Z_{v\_tot\alpha\beta c22}$ in $\omega > \omega_{\rm LPFX} + \omega_0$, which helps to boost the phase angle of $Z_{v\_tot\alpha\beta c22}$, and hence, improve the stability of the FCIVI loop.
2) $G_{\rm LPF}R$: In contrast to $G_{\rm LPF}X$, the magnitude of the real part of $Z_{v\_tot\alpha\beta c22}$ will be reduced by $G_{\rm LPF}R$ in $\omega > \omega_{\rm LPFR} + \omega_0$, which introduces additional phase lag of $Z_{v\_tot\alpha\beta c22}$ and would also jeopardize the stability of the FCIVI loop.
3) $G_{\rm LPF}i$: It can be seen from (27) that the magnitude of both the real and imaginary part of $Z_{v\_tot\alpha\beta c22}$ will be reduced by $G_{\rm LPF}i$ in a similar manner when $\omega > \omega_{\rm LPFi} + \omega_0$. Thus, $G_{\rm LPF}i$ would have a limited impact on the phase angle of $Z_{v\_tot\alpha\beta c22}$, so as the stability of the FCIVI loop.

Therefore, only $G_{\rm LPF}X$ will be adopted for implementing adaptive VI, due to its positive impact on system stability. Hence, (27) can be simplified as

$$Z_{v\_tot\alpha\beta c22}(s) = G_{\rm HPF}(s-j\omega_0)R_{\rm ad} + \left(R_{v0} + \frac{k_R I_{\rm mag0}}{2}\right) - jn_{X/R}G_{LPFX}(s-j\omega_0)\left(R_{v0} + \frac{k_R I_{\rm mag0}}{2}\right). \quad (28)$$

Then, $\omega_{\rm LPF}X$ should be carefully tuned to guarantee that $T_{\rm coup}$ satisfies the Nyquist stability criterion, which will be elaborated in the following.

The magnitude of $T_{\rm coup}$ is unity at its magnitude crossover frequency ω_c, i.e.,

$$|T_{\rm coup}(j\omega_c)| = 1. \quad (29)$$

Substituting (25) and (28) into (29), and the result is given by (30) at the bottom of the next page.

It should be noted that the cutoff frequency of G_{HPF} is usually selected around several Hz to guarantee a wide frequency range of active damping [2], [24], and hence, G_{HPF} can be approximated as unity gain at ω_c. On the other hand, $\omega_{\mathrm{LPF}X}$ should be tuned to be much less than $\omega_c - \omega_0$ to minimize $\mathrm{Im}[Z_{v\_\mathrm{tot}\alpha\beta c22}(j\omega_c)]$ for the phase margin (PM) improvement, e.g.,

$$\omega_{\mathrm{LPF}X} < \frac{1}{10}\left(\omega_c - \omega_0\right). \tag{31}$$

Therefore, $G_{\mathrm{LPF}X}(s - j\omega_0)$ can be approximated as follows at ω_c:

$$G_{\mathrm{LPF}X}\left(j\omega_c - j\omega_0\right) = \frac{\omega_{\mathrm{LPF}X}}{j\left(\omega_c - \omega_0\right) + \omega_{\mathrm{LPF}X}} \approx \frac{\omega_{\mathrm{LPF}X}}{j\left(\omega_c - \omega_0\right)}. \tag{32}$$

Substituting (32) into (30), which leads to

$$\left|T_{\mathrm{coup}}\left(j\omega_c\right)\right| \approx \frac{R_{\mathrm{ad}} + \left(1 - \frac{n_{X/R}\omega_{\mathrm{LPF}X}}{\omega_c - \omega_0}\right)\left(R_{v0} + \frac{k_R I_{\mathrm{mag0}}}{2}\right)}{\left(\omega_c - 2\omega_0\right)L_f} = 1. \tag{33}$$

Solving $\omega_{\mathrm{LPF}X}$ from (33), which yields

$$\omega_{\mathrm{LPF}X} = \frac{\omega_c - \omega_0}{n_{X/R}\left(R_{v0} + \frac{k_R I_{\mathrm{mag0}}}{2}\right)} \cdot \left[R_{\mathrm{ad}} + R_{v0} + \frac{k_R I_{\mathrm{mag0}}}{2} - \left(\omega_c - 2\omega_0\right)L_f\right]. \tag{34}$$

Since $\omega_{\mathrm{LPF}X} \geq 0$, the maximum value of ω_c can be calculated from (34), i.e.,

$$\omega_{c\max} = 2\omega_0 + \frac{1}{L_f}\left(R_{\mathrm{ad}} + R_{v0} + \frac{k_R I_{\mathrm{mag0}}}{2}\right). \tag{35}$$

Based on the Nyquist stability criterion, the FCIVI loop is stable provided the phase angle of T_{coup} does not cross $-180°$ in the frequency range $[2\omega_0, \omega_c]$, i.e.,

$$\angle T_{\mathrm{coup}}\left(j\omega\right) > -180°, \omega \in [2\omega_0, \omega_c]. \tag{36}$$

Substituting (25) and (28) into (36), which yields

$$\omega_{\mathrm{LPF}X} < \frac{\left(\omega - \omega_0\right)\left(1 - \sqrt{1 - 4b}\right)}{2a} = f\left(\omega\right), \omega \in [2\omega_0, \omega_c] \tag{37}$$

where

$$a = \frac{\left(R_{\mathrm{ad}} + R_{v0} + \frac{k_R I_{\mathrm{mag0}}}{2}\right)}{n_{X/R}\left(R_{v0} + \frac{k_R I_{\mathrm{mag0}}}{2}\right)} - \frac{1}{K} \tag{38.1}$$

$$b = \frac{\left(R_{\mathrm{ad}} + R_{v0} + \frac{k_R I_{\mathrm{mag0}}}{2}\right)^2}{n_{X/R}^2\left(R_{v0} + \frac{k_R I_{\mathrm{mag0}}}{2}\right)^2} - \frac{\left(R_{\mathrm{ad}} + R_{v0} + \frac{k_R I_{\mathrm{mag0}}}{2}\right)}{n_{X/R}K\left(R_{v0} + \frac{k_R I_{\mathrm{mag0}}}{2}\right)} \tag{38.2}$$

$$K = \cot\left[\left(\omega_{c\max} - 2\omega_0\right)T_d\right]. \tag{38.3}$$

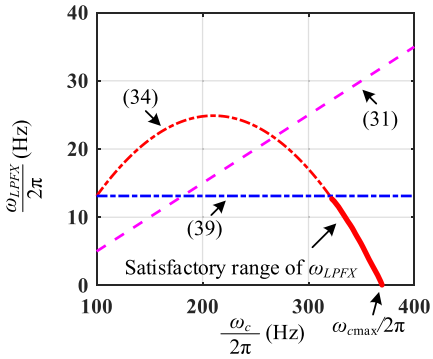

Fig. 7. Range of $\omega_{\mathrm{LPF}X}$ that guarantees the stability of $T_{\mathrm{coup}}(s)$.

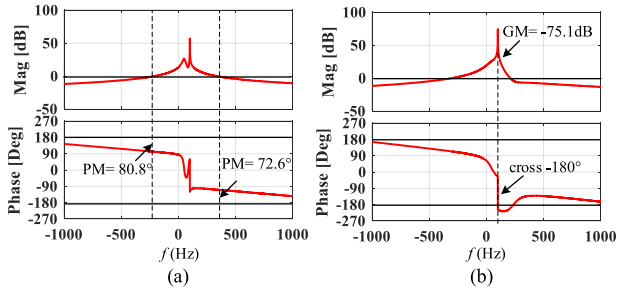

Fig. 8. Bode diagram of $T_{\mathrm{coup}}(s)$ with $G_{\mathrm{LPF}X}$ only. (a) $\omega_{\mathrm{LPF}X} = 2\pi{\cdot}10$ (rad/s), stable. (b) $\omega_{\mathrm{LPF}X} = 2\pi{\cdot}50$ (rad/s), unstable.

Since a and b in (38) are constant values, it is known from (37) that $f(\omega)$ reaches its minimum when $\omega = 2\omega_0$. Therefore, (36) can be satisfied if and only if $\omega_{\mathrm{LPF}X} < f(2\omega_0)$, i.e.,

$$\omega_{\mathrm{LPF}X} < f\left(2\omega_0\right) = \frac{\omega_0\left(1 - \sqrt{1 - 4b}\right)}{2a} = \omega_{\mathrm{LPF}X\_\max}. \tag{39}$$

Fig. 7 visualizes the relationship between $\omega_{\mathrm{LPF}X}$ and ω_c based on (34), as well as other constraints of $\omega_{\mathrm{LPF}X}$ given by (31) and (39). The bold solid curve in Fig. 7 highlights the range of $\omega_{\mathrm{LPF}X}$ that satisfies (31), (34), and (39) so as to guarantee the stability of the FCIVI loop. Based on parameters given in Table I, this range is calculated as (0 rad/s, $2\pi{\cdot}13.1$ rad/s).

Fig. 8 shows the bode diagram of T_{coup} with $G_{\mathrm{LPF}X}$ only, and $\omega_{\mathrm{LPF}X}$ is selected as $2\pi{\cdot}10$ (rad/s) in Fig. 8(a) and $2\pi{\cdot}50$ (rad/s) in Fig. 8(b). It is clear that the FCIVI loop is stable when

$$\left|T_{\mathrm{coup}}\left(j\omega_c\right)\right| = \frac{\left|e^{-j(\omega_c - 2\omega_0)T_d}\right|}{\left(\omega_c - 2\omega_0\right)L_f}\left|G_{\mathrm{HPF}}\left(j\omega_c - j\omega_0\right)R_{\mathrm{ad}} + \left(R_{v0} + \frac{k_R I_{\mathrm{mag0}}}{2}\right) - jn_{X/R}G_{\mathrm{LPF}X}\left(j\omega_c - j\omega_0\right)\left(R_{v0} + \frac{k_R I_{\mathrm{mag0}}}{2}\right)\right| = \frac{\left|G_{\mathrm{HPF}}\left(j\omega_c - j\omega_0\right)R_{\mathrm{ad}} + \left(R_{v0} + \frac{k_R I_{\mathrm{mag0}}}{2}\right) - jn_{X/R}G_{\mathrm{LPF}X}\left(j\omega_c - j\omega_0\right)\left(R_{v0} + \frac{k_R I_{\mathrm{mag0}}}{2}\right)\right|}{\left(\omega_c - 2\omega_0\right)L_f} = 1 \tag{30}$$

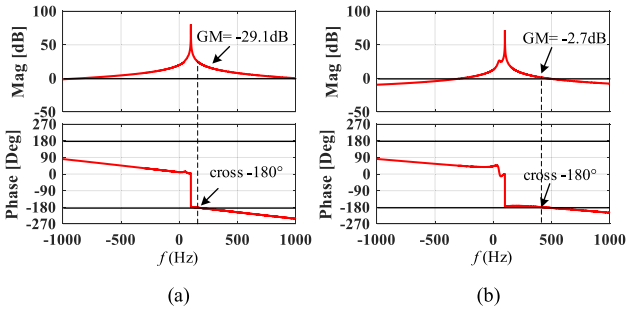

Fig. 9. Bode diagram of $T_{\rm coup}(s)$. (a) With $G_{{\rm LPF}R}$ only, $\omega_{{\rm LPF}R} = 2\pi{\cdot}10$ (rad/s), unstable. (b) With $G_{{\rm LPF}i}$ only, $\omega_{{\rm LPF}i} = 2\pi{\cdot}10$ (rad/s), unstable.

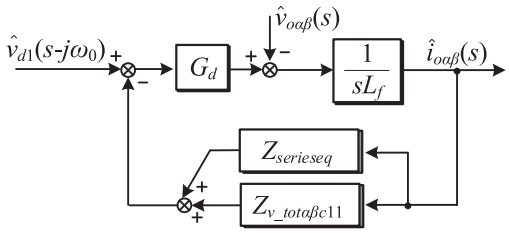

Fig. 10. Equivalent representation of the adaptive VI loop.

$\omega_{{\rm LPF}X}$ is selected in the range given in Fig. 7, as dictated by the positive PM of $T_{\rm coup}$ given by Fig. 8(a). Otherwise it might be unstable, as shown in Fig. 8(b). The results given in Fig. 8 verify the effectiveness of the proposed parameters tuning method.

In order to visualize the impact of $G_{{\rm LPF}R}$ and $G_{{\rm LPF}i}$ on the stability of the FCIVI loop, Fig. 9(a) and (b) shows the bode diagram of $T_{\rm coup}$ with $G_{{\rm LPF}R}$ only ($G_{{\rm LPF}i}$ only) and $\omega_{{\rm LPF}R}$ $= 2\pi{\cdot}10$ (rad/s) [$\omega_{{\rm LPF}i} = 2\pi{\cdot}10$ (rad/s)]. The negative GM of $T_{\rm coup}$ can be observed no matter $G_{{\rm LPF}R}$ or $G_{{\rm LPF}i}$ is adopted, indicating that none of these LPFs are capable of stabilizing the FCIVI loop, which is in accordance with the analysis presented at the beginning of this part.

B. Stabilizing Adaptive VI Loop

As dictated by (23) and Fig. 5(b), the FCIVI loop emulates an additional VI $Z_{\rm serieseq}$ that is series connected with $Z_{v\_tot\alpha\beta c11}$. Therefore, the adaptive VI loop given in Fig. 4 can be equivalent as that given in Fig. 10, based on which, its open-loop gain $T_{\rm AVI}$ is expressed as

$$T_{\rm AVI} = \frac{G_d(s)}{sL_f}\left[Z_{v\_tot\alpha\beta c11}(s) + Z_{\rm serieseq}(s)\right] \tag{40}$$

where

$$Z_{v\_tot\alpha\beta c11}(s) = G_{\rm HPF}(s-j\omega_0)R_{\rm ad} + \left(R_{v0} + \frac{k_R I_{\rm mag0}}{2}\right) + jn_{X/R}G_{{\rm LPF}X}(s-j\omega_0)\left(R_{v0} + \frac{k_R I_{\rm mag0}}{2}\right). \tag{41}$$

It is known from (40) that the term $1/(sL_f)$ would introduce 90° phase shift in the negative frequency range ($\omega < 0$), in which the additional phase leading would be further yielded due to the delay term $G_d(s)$. Therefore, $T_{\rm AVI}(s)$ is prone to crossing over 180° in $\omega < 0$ if phase angle of $Z_{v\_tot\alpha\beta c11}(s)$ approximates

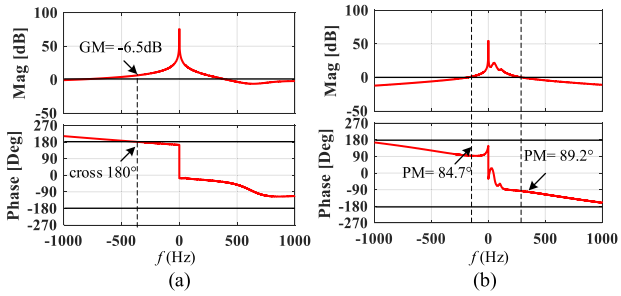

Fig. 11. Bode diagram of $T_{\rm AVI}(s)$. (a) Without $G_{{\rm LPF}X}$, unstable. (b) With $G_{{\rm LPF}X}$ and $\omega_{{\rm LPF}X} = 2\pi{\cdot}10$ (rad/s), stable.

90°, which corresponds to the case that $G_{{\rm LPF}X}$ is not adopted, see (41). Fig. 11(a) shows the bode diagram of $T_{\rm AVI}(s)$ without $G_{{\rm LPF}X}$, where a negative gain margin (GM $= -6.5$ dB) can be clearly observed, indicating the instability of the adaptive VI loop.

Therefore, $G_{{\rm LPF}X}$ turns out to be crucial in stabilizing both the FCIVI and the adaptive VI loop. Yet, it is nontrivial to formulate an analytic design guideline of $\omega_{{\rm LPF}X}$ for stabilizing the adaptive VI loop, due to the complex representation of $Z_{\rm serieseq}$ in (40). Hence, a trial-and-error method is adopted in this part, i.e., $\omega_{{\rm LPF}X}$ is first selected as its maximum possible value based on Fig. 7 to guarantee the stability of the FCIVI loop. Then, it is gradually reduced until the adaptive VI loop becomes stable i.e., $T_{\rm AVI}(s)$ satisfies the Nyquist stability criterion.

It is known from Fig. 7 that $\omega_{{\rm LPF}X\_\max} = 2\pi{\cdot}13.1$ (rad/s). Based on the parameters given in Table I, the adaptive VI loop is already stable even with $\omega_{{\rm LPF}X} = \omega_{{\rm LPF}X\_\max}$, and hence, $\omega_{{\rm LPF}X} = 2\pi{\cdot}10$ (rad/s) is selected in this article. Fig. 11(b) shows the bode diagram of $T_{\rm AVI}(s)$ with $\omega_{{\rm LPF}X} = 2\pi{\cdot}10$ (rad/s), where a positive PM can be clearly observed.

To further provide a holistic illustration on the parametric impact of different LPFs on the stability of the adaptive VI loop, Fig. 12 shows the root loci of the adaptive VI loop with different LPFs in respect to variations of their cutoff frequencies from 5 to 100 Hz (for clarity, only dominant poles of the system are given). It can be observed from Fig. 12(a) that the adaptive VI loop can be stabilized with $G_{{\rm LPF}X}$ only, as the dominant poles move from the RHP to the left-half plane with the reduced cutoff frequency of $G_{{\rm LPF}X}$. The critical cutoff frequency of $G_{{\rm LPF}X}$ beyond which the system is unstable is identified as $\omega_{{\rm LPF}X\_critical} = 2\pi{\cdot}20.4$ (rad/s). It is noted that $\omega_{{\rm LPF}X\_critical}$ is a little bit higher than $\omega_{{\rm LPF}X\_\max}$ calculated in (39), which is not surprising since the simplification adopted in (32) would lead to a little bit conservative prediction of $\omega_{{\rm LPF}X\_\max}$. On the other hand, even though the dominant poles also move leftwards with the reduced cutoff frequency of $G_{{\rm LPF}i}$, it is still in the RHP even a very small cutoff frequency [i.e., $\omega_{{\rm LPF}i} = 2\pi{\cdot}5$ (rad/s)] is adopted, see Fig. 12(b). Hence, the adaptive VI loop can hardly be stabilized by using $G_{{\rm LPF}i}$ only. Moreover, using $G_{{\rm LPF}R}$ only cannot stabilize the adaptive VI loop either. As shown in Fig. 12(c), the dominant poles are always in the RHP and their positions are hardly affected by the cutoff frequency of $G_{{\rm LPF}R}$.

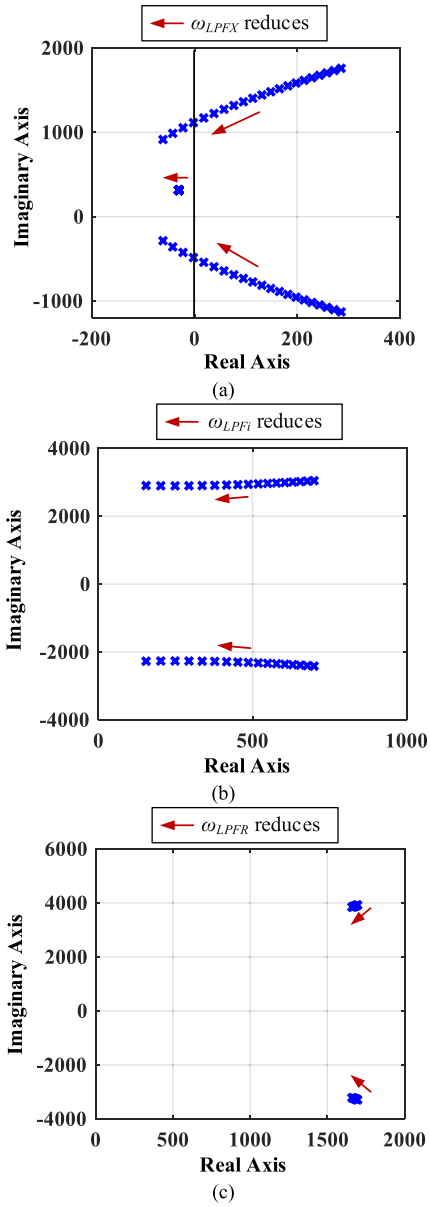

Fig. 12. Root loci of the adaptive VI loop with different LPFs. (a) With $G_{\mathrm{LPF}\,X}$ only, and $\omega_{\mathrm{LPF}\,X}$ is reduced from $2\pi{\cdot}100$ to $2\pi{\cdot}5$ (rad/s). (b) With $G_{\mathrm{LPF}\,i}$ only, and $\omega_{\mathrm{LPF}\,i}$ is reduced from $2\pi{\cdot}100$ to $2\pi{\cdot}5$ (rad/s). (c) With $G_{\mathrm{LPF}\,R}$ only, and $\omega_{\mathrm{LPF}\,R}$ is reduced from $2\pi{\cdot}100$ to $2\pi{\cdot}5$ (rad/s).

V. Small-Signal Modeling and Parameters Tuning of Outer Loops

After stabilizing the adaptive VI loop, the parameters of outer loops, i.e., APC/RPC loops and the SLVM control loop should be further tuned to guarantee the stable operation of GFM-VSC in both the steady-state and fault conditions. Yet, it is known from Fig. 1 that the output of the SLVM control, i.e., V_{d1}, will be saturated during grid faults as $V_{o\mathrm{mag}}{<}V_{d\mathrm{ref}}$, which naturally bypasses the RPC and the SLVM control. Hence, the parameters tuning of the RPC loop and the SLVM control loop only need to consider the steady-state operation of GFM-VSC without adaptive VI, which is well documented in [22], [23].

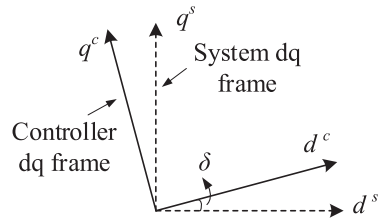

Fig. 13. Controller *dq* frame and system *dq* frame.

On the other hand, the parameters tuning of the APC loop should consider the dynamics of adaptive VI as APC still operates during grid faults, which will be detailed in the following.

A. Small-Signal Modeling of the APC Loop Considering Dynamics of Adaptive VI

By considering the dynamics of the APC, there are two rotating *dq* frames of GFM-VSC [24]: one is the *controller-dq* frame that is defined by the output phase angle of the APC, and another is the *system-dq* frame that is aligned with phase angle of the grid voltage, as shown in Fig. 13. For clarity, superscript *s* represents the variables in the *system-dq* frame, while the superscript *c* denotes the variables in the *controller-dq* frame.

Define δ as the phase angle difference between the *controller-dq* frame and the *system-dq* frame, i.e., $\delta = \theta_{\mathrm{ref}} - \theta_g$. Then the relationships between the state variables in the *controller-dq* frame and the *system-dq* frame are given by

$$x_{dq}^{c} = e^{-j\delta} x_{dq}^{s}. \tag{42}$$

The small-signal representation of (42) is expressed as

$$\begin{aligned}\hat{x}_{dq}^{c} &= e^{-j\delta_0}\hat{x}_{dq}^{s} - jX_{dq0}^{s}e^{-j\delta_0}\hat{\delta} \Leftrightarrow \\ \begin{bmatrix}\hat{x}_d^c \\ \hat{x}_q^c\end{bmatrix} &= \begin{bmatrix}\cos\delta_0 & \sin\delta_0 \\ -\sin\delta_0 & \cos\delta_0\end{bmatrix}\begin{bmatrix}\hat{x}_d^s \\ \hat{x}_q^s\end{bmatrix} \\ &\quad + \hat{\delta}\begin{bmatrix}\cos\delta_0 & \sin\delta_0 \\ -\sin\delta_0 & \cos\delta_0\end{bmatrix}\begin{bmatrix}X_{q0}^{s} \\ -X_{d0}^{s}\end{bmatrix}.\end{aligned} \tag{43}$$

It is known from (15) that the dynamics of inverter bridge voltage in the *controller-dq* frame can be expressed as ($\hat{v}_{d1} = 0$ due to the saturation of the SLVM control, and the control delay is also omitted due to its limited impact on low-frequency dynamics that is of concern when designing APC [22]–[24])

$$\begin{bmatrix}\hat{v}_{\mathrm{inv}d}^{c} \\ \hat{v}_{\mathrm{inv}q}^{c}\end{bmatrix} = \begin{bmatrix}\hat{m}_d^c \\ \hat{m}_q^c\end{bmatrix} = -\mathbf{Z}_{\mathbf{v\_totdq}}\begin{bmatrix}\hat{i}_{od}^{c} \\ \hat{i}_{oq}^{c}\end{bmatrix}. \tag{44}$$

Transform (44) to the system-*dq* frame based on (43), which yields

$$\begin{aligned}\begin{bmatrix}\hat{v}_{\mathrm{inv}d}^{s} \\ \hat{v}_{\mathrm{inv}q}^{s}\end{bmatrix} &= -\mathbf{Z}_{\mathbf{v\_totdq}}\begin{bmatrix}\hat{i}_{od}^{s} \\ \hat{i}_{oq}^{s}\end{bmatrix} \\ &\quad + \left(\mathbf{Z}_{\mathbf{v\_totdq}}\begin{bmatrix}-I_{oq0}^{s} \\ I_{od0}^{s}\end{bmatrix} + \begin{bmatrix}-V_{\mathrm{inv}q0}^{s} \\ V_{\mathrm{inv}d0}^{s}\end{bmatrix}\right)\hat{\delta}.\end{aligned} \tag{45}$$

It is known from [23] that the output capacitor branch in Fig. 1 can be treated as open circuit when designing the APC due to its large impedance in the low-frequency range. Therefore, the

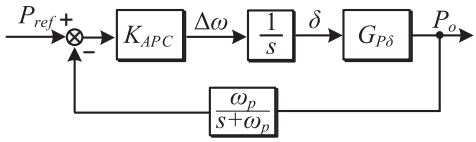

Fig. 14. Block diagram of the APC loop.

circuit dynamics can be expressed as

$$\begin{bmatrix} v^s_{\text{inv}d} \\ v^s_{\text{inv}q} \end{bmatrix} - \begin{bmatrix} v^s_{gd} \\ v^s_{gq} \end{bmatrix} = \underbrace{\begin{bmatrix} sL & -\omega_0 L \\ \omega_0 L & sL \end{bmatrix}}_{\mathbf{Z}_L} \begin{bmatrix} i^s_{od} \\ i^s_{oq} \end{bmatrix} \tag{46.1}$$

$$\begin{bmatrix} v^s_{od} \\ v^s_{oq} \end{bmatrix} - \begin{bmatrix} v^s_{gd} \\ v^s_{gq} \end{bmatrix} = \underbrace{\begin{bmatrix} sL_g & -\omega_0 L_g \\ \omega_0 L_g & sL_g \end{bmatrix}}_{\mathbf{Z}_{L_g}} \begin{bmatrix} i^s_{od} \\ i^s_{oq} \end{bmatrix} \tag{46.2}$$

where

$$L = L_f + L_g. \tag{47}$$

Considering $\hat{v}^s_{gd} = 0$ and $\hat{v}^s_{gq} = 0$. The small-signal representation of (46) is given by

$$\begin{bmatrix} \hat{v}^s_{\text{inv}d} \\ \hat{v}^s_{\text{inv}q} \end{bmatrix} = \mathbf{Z}_L \begin{bmatrix} \hat{i}^s_{od} \\ \hat{i}^s_{oq} \end{bmatrix} \tag{48.1}$$

$$\begin{bmatrix} \hat{v}^s_{od} \\ \hat{v}^s_{oq} \end{bmatrix} = \mathbf{Z}_{L_g} \begin{bmatrix} \hat{i}^s_{od} \\ \hat{i}^s_{oq} \end{bmatrix}. \tag{48.2}$$

Substituting (48.1) into (45), which yields

$$\begin{bmatrix} \hat{i}^s_{od} \\ \hat{i}^s_{oq} \end{bmatrix} = \underbrace{\left(\mathbf{Z}_L + \mathbf{Z}_{\mathbf{v\_tot dq}}\right)^{-1} \left(\mathbf{Z}_{\mathbf{v\_tot dq}} \begin{bmatrix} -I^s_{oq0} \\ I^s_{od0} \end{bmatrix} + \begin{bmatrix} -V^s_{\text{inv}q0} \\ V^s_{\text{inv}d0} \end{bmatrix} \right)}_{\mathbf{G}_{\mathbf{i}\delta}} \hat{\delta}. \tag{49}$$

The output active power of GFM-VSC is calculated as [23]

$$p_o = \frac{3}{2}\left(v^s_{od} i^s_{od} + v^s_{oq} i^s_{oq}\right). \tag{50}$$

The small-signal representation of (50) is given by

$$\hat{p}_o = \frac{3}{2}\left(\begin{bmatrix} V^s_{od0} & V^s_{oq0} \end{bmatrix} \begin{bmatrix} \hat{i}^s_{od} \\ \hat{i}^s_{oq} \end{bmatrix} + \begin{bmatrix} I^s_{od0} & I^s_{oq0} \end{bmatrix} \begin{bmatrix} \hat{v}^s_{od} \\ \hat{v}^s_{oq} \end{bmatrix} \right). \tag{51}$$

Substituting (48.2) and (49) into (51), which yields

$$G_{P\delta} = \frac{\hat{p}_o}{\hat{\delta}} = \frac{3}{2}\left(\begin{bmatrix} V^s_{od0} & V^s_{oq0} \end{bmatrix} + \begin{bmatrix} I^s_{od0} & I^s_{oq0} \end{bmatrix} \mathbf{Z}_{L_g} \right) \mathbf{G}_{\mathbf{i}\delta}. \tag{52}$$

Fig. 14 shows the block diagram of the APC loop, and its loop gain can be derived as

$$T_{\text{APC}} = \frac{K_{\text{APC}}}{s} \frac{\omega_p}{s+\omega_p} G_{P\delta}(s). \tag{53}$$

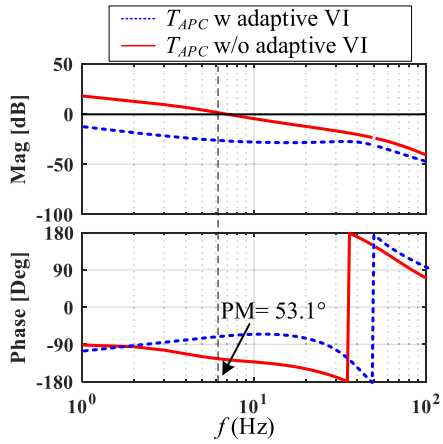

Fig. 15. Bode diagram of APC with and without adaptive VI.

B. Impact of Adaptive VI Loop on Parameters Tuning of APC Loop

It is known from [7], [35], and [36] that the stability of GFM-VSC is degraded under stiffer grid conditions, and hence, the worst case, i.e., $L_g = 0$, is considered here for designing the APC loop. Therefore, (52) can be simplified as

$$G_{P\delta} = \frac{3}{2}\left[V^s_{od0} \; V^s_{oq0} \right] \mathbf{G}_{\mathbf{i}\delta}. \tag{54}$$

As the starting point, the parameters of the APC loop are tuned to guarantee the stability of GFM-VSC under the steady-state operation where the adaptive VI is not activated. In this case, (54) can be further deduced as [7]

$$G_{P\delta} = \frac{3}{2} \frac{V_{om} V_{\text{inv}m} \left(-sL \sin\delta_0 + \omega_0 L \cos\delta_0\right)}{\left(G_{\text{HPF}} R_{ad} + sL\right)^2 + \left(\omega_0 L\right)^2} \tag{55}$$

where V_{om} and $V_{\text{inv}\,m}$ represent the magnitude of output voltage and inverter bridge voltage, respectively.

It is known from Fig. 14 that there are two parameters, i.e., K_{APC} and ω_p, to be tuned. K_{APC} represents the P–ω droop coefficient and its value is usually determined by the grid code. In this article, $K_{\text{APC}} = 0.02$ p.u. is selected based on the requirement of EN 50438 [37]. On the other hand, ω_p should be tuned to guarantee enough PM of T_{APC}. Following the design guideline given in [22]–[24], $\omega_p = 2\pi{\cdot}50$ (rad/s) is selected in this article. The bode diagram of T_{APC} during the steady-state operation of GFM-VSC is dictated by the solid line in Fig. 15, where a positive PM (PM = 53.1°) can be clearly observed.

Then, further investigation is performed to check whether the APC loop is still stable during grid faults. The dashed line in Fig. 15 illustrates the bode diagram of T_{APC} during grid faults. It can be seen that the magnitude of T_{APC} is reduced in this scenario, indicating even better stability performance compared with that during the steady-state operation. The loop gain reduction of T_{APC} can be intuitively understood from (55). During grid faults, the numerator of (55) will be reduced due to the reduced output voltage and inverter bridge voltage. In contrast, the denominator of (55) will be increased due to the additional VI introduced by the adaptive VI control. Hence, both

TABLE II
CONTROLLER PARAMETERS

SYMBOL	DESCRIPTION	VALUE (P.U.)
$n_{X/R}$	X/R ratio of the adaptive VI	5
k_R	Proportional gain of adaptive virtual resistor	0.29 p.u.
I_{th}	Threshold current of activating adaptive VI	1.1 p.u.
I_{lim}	Current limit	1.5 p.u.
K_{iv}	Integral gain of SLVM control	6.28 p.u.
ω_{LPFX}	Cutoff frequency of G_{LPFX}.	0.2 p.u.
R_{ad}	Active damping resistor	0.1 p.u.
ω_{HPF}	Cutoff frequency of G_{HPF}.	0.1 p.u.
K_{APC}	P-ω droop control	0.02 p.u.
ω_p	Cutoff frequency of G_{LPFp}	1 p.u.
K_{RPC}	Q-V droop control	0.1 p.u.
ω_q	Cutoff frequency of G_{LPFq}	1 p.u.

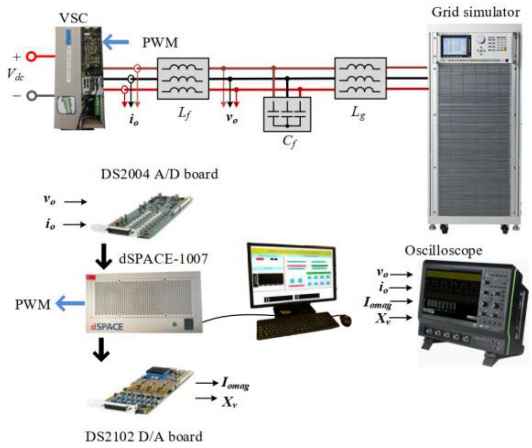

Fig. 16. Configuration of the experimental setup.

the smaller numerator and larger denominator contribute to the reduction of $G_{P\delta}$ during grid faults, so as to T_{APC}.

The analysis in this section highlights that even though the dynamics of the APC loop is affected by adaptive VI during grid faults, its stability is not jeopardized. Hence, parameters tuning of the APC loop can still follow the guideline given in previous article that considering the steady-state operation of GFM-VSC only.

Based on abovementioned design guidelines, parameters of different control loops of GFM-VSC can be finally calculated, as listed in Table II.

C. Discussion

It is noted that the proposed controller parameters tuning method is based on the small-signal model of GFM-VSC that is developed by linearizing the system at the specific operating point. Therefore, this method can be adopted to guarantee a stable operating point of GFM-VSC during grid faults, which is the precondition (necessary condition) for a stable FRT. Yet, GFM-VSC may still fail to converge to this stable operating point during grid faults, due to its nonlinear behavior that cannot be captured in the small-signal model. This convergence issue should be further assessed by performing large-signal stability analysis, which will be investigated in our future article.

VI. SIMULATION AND EXPERIMENTAL RESULTS

The nonlinear time-domain simulations and experimental tests are carried out to validate the small-signal model and the proposed parameters tuning method for GFM-VSC. The parameters given in in Tables I and II are adopted in simulation and experimental tests. The simulation is performed on the switching model of a three-phase VSC in MATLAB/Simulink, which is set as the same as the experiment.

Fig. 16 illustrates the configuration of the experimental setup, where the control algorithm is implemented in the DS1007 dSPACE system. In order to capture the dynamic impact of adaptive VI on the current limitation performance, X_v and $I_{o\mathrm{mag}}$, that are calculated based on (3) and (7), are outputted through the DS2102 high-speed D/A board and then sent to the oscilloscope for measurement.

A. Verifications on the Small-Signal Model

Based on the small-signal model developed in Section V, the output impedance matrix of GFM-VSC with adaptive VI in $\alpha\beta$ frame can be calculated as (see Appendix A for the detailed deviation process)

$$\begin{bmatrix} \hat{v}_{o\alpha\beta}(s) \\ \hat{v}^*_{o\alpha\beta}(s-2j\omega_0) \end{bmatrix} = \underbrace{\begin{bmatrix} Z_{\mathrm{GFM}\alpha\beta 11}(s) & Z_{\mathrm{GFM}\alpha\beta 12}(s) \\ Z_{\mathrm{GFM}\alpha\beta 21}(s) & Z_{\mathrm{GFM}\alpha\beta 22}(s) \end{bmatrix}}_{\mathbf{Z}_{\mathrm{GFM}\alpha\beta}(s)} \begin{bmatrix} \hat{i}_{o\alpha\beta}(s) \\ \hat{i}^*_{o\alpha\beta}(s-2j\omega_0) \end{bmatrix}. \tag{56}$$

In order to verify the accuracy of the theoretical model, impedance measurement of GFM-VSC with adaptive VI is performed in MATLAB/Simulink, and the results are given by blue circles in Fig. 17. It can be seen that the impedance measurement results match well with theoretical calculations, which verifies the accuracy of the developed small-signal model.

B. Verifications on Small-Signal Stability Analysis

To verify the small-signal stability analysis results given in Section IV, the experimental tests are performed by operating GFM-VSC under the same operating point that is used in the theoretical analysis ($V_g = 0.2$ p.u.), and the adaptive VI is activated in this scenario to avoid the overcurrent of GFM-VSC. As shown in Fig. 18, the GFM-VSC is initially operated stably with $G_{\mathrm{LPF}X}$ only and $\omega_{\mathrm{LPF}X} = 2\pi{\cdot}10$ (rad/s) $< \omega_{\mathrm{LPF}X\_\mathrm{critical}}$. Yet, it becomes unstable by increasing $\omega_{\mathrm{LPF}X}$ to $2\pi{\cdot}50$ (rad/s) that is beyond $\omega_{\mathrm{LPF}X\_\mathrm{critical}}$, which is dictated by amplified oscillations in the voltage and current of VSC, as shown in Fig. 18(a), and VSC is finally blocked to avoid the damage. The experimental tests confirm the stability analysis given by Fig. 12(a).

Moreover, small-signal stability analysis given by Fig. 12(b) and (c) reveal that GFM-VSC cannot be stabilized with $G_{\mathrm{LPF}R}$ or $G_{\mathrm{LPF}i}$ only. Those predictions are verified by experimental

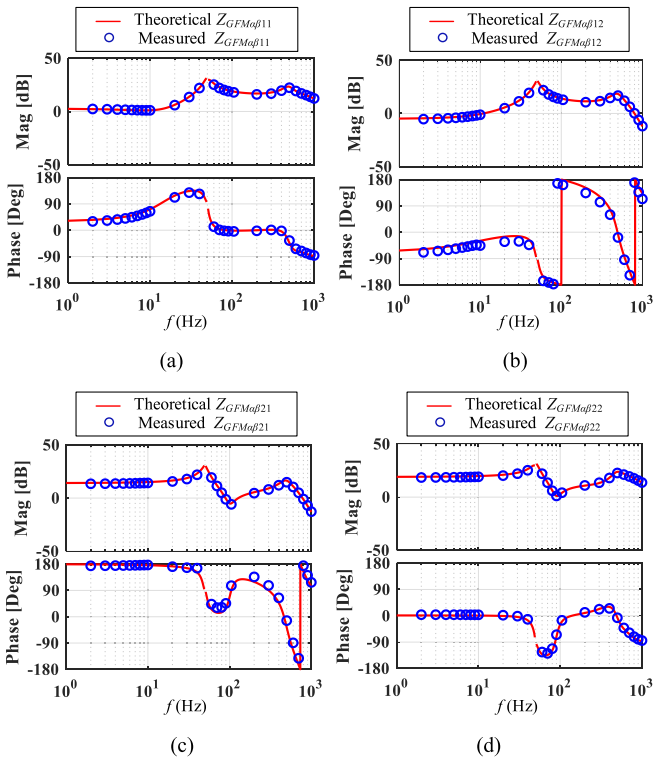

Fig. 17. Theoretically calculated and measured output impedance matrix of GFM-VSC with adaptive VI in $\alpha\beta$ frame. (a) $Z_{\mathrm{GFM}\alpha\beta 11}$. (b) $Z_{\mathrm{GFM}\alpha\beta 12}$. (c) $Z_{\mathrm{GFM}\alpha\beta 21}$. (d) $Z_{\mathrm{GFM}\alpha\beta 22}$.

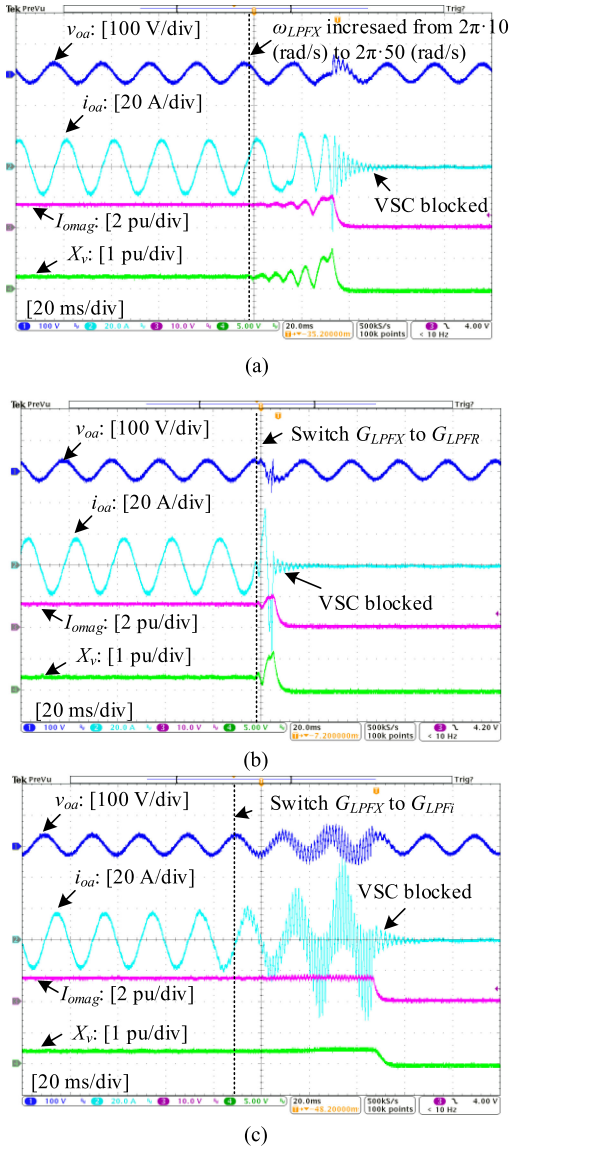

Fig. 18. Experimental results of GFM-VSC operating under $V_g = 0.2$ p.u, and GFM-VSC is initially operated with $G_{\mathrm{LPF}X}$ only with $\omega_{\mathrm{LPF}X} = 2\pi{\cdot}10$ (rad/s). (a) Cutoff frequency of $G_{\mathrm{LPF}X}$ is increased from 10 to 50 Hz. (b) Switch $G_{\mathrm{LPF}X}$ with $\omega_{\mathrm{LPF}X} = 2\pi{\cdot}10$ (rad/s) to $G_{\mathrm{LPF}R}$ with $\omega_{\mathrm{LPF}R} = 2\pi{\cdot}10$ (rad/s). (c) Switch $G_{\mathrm{LPF}X}$ with $\omega_{\mathrm{LPF}X} = 2\pi{\cdot}10$ (rad/s) to $G_{\mathrm{LPF}i}$ with $\omega_{\mathrm{LPF}i} = 2\pi{\cdot}10$ (rad/s).

results given in Fig. 18(b) and (c). It can be seen that GFM-VSC becomes unstable after switching $G_{\mathrm{LPF}X}$ to $G_{\mathrm{LPF}R}$ or $G_{\mathrm{LPF}i}$, even though a very small cutoff frequency is used in $G_{\mathrm{LPF}R}$ or $G_{\mathrm{LPF}i}$ [$\omega_{\mathrm{LPF}R} = 2\pi{\cdot}10$ (rad/s), $\omega_{\mathrm{LPF}i} = 2\pi{\cdot}10$ (rad/s)].

C. Tests of GFM-VSC Under Large Disturbances

Fig. 19 shows the dynamic response of GFM-VSC during grid faults where V_g drops from 1 to 0.2 p.u. As pointed out in Section V-C, having a stable operation point during grid faults is the precondition (necessary condition) for the large-signal stability, i.e., the unstable FRT is inevitable if the system is small-signal unstable at $V_g = 0.2$ p.u., which corresponds to cases that no LPFs is adopted in adaptive VI, using only $G_{\mathrm{LPF}R}$ or $G_{\mathrm{LPF}i}$ in adaptive VI, or using $G_{\mathrm{LPF}X}$ in adaptive VI with too high cutoff frequency ($\omega_{\mathrm{LPF}X} > \omega_{\mathrm{LPF}X\_\mathrm{critical}}$), as verified by experimental results in Fig. 19(a)–(d).

The theoretical analysis and experimental test have verified that GMF-VSC is small-signal stable at $V_g = 0.2$ p.u. by adopting $G_{\mathrm{LPF}X}$ only with $\omega_{\mathrm{LPF}X} = 2\pi{\cdot}10$ (rad/s) $< \omega_{\mathrm{LPF}X\_\mathrm{critical}}$. The experimental test given in Fig. 19(e) shows that a stable FRT of GFM-VSC can also be guaranteed with these controller parameter settings. It can be seen that the adaptive VI is automatically activated during grid faults, and the steady-state fault current is limited to 1.5 p.u. as expected. The overshoot of fault current with a peak value around 1.9 p.u. can also be observed at the instant of grid faults. This is acceptable as VSC is usually designed with the capability to withstand 2.0 p.u. current within a short period [5]. Nevertheless, the theoretical justification of this stable FRT should be made based on the large-signal stability analysis, which is our future work.

In practice, not only the grid voltage, but also the equivalent grid impedance would change during grid faults due to the impact of the fault impedance. In order to further investigate the performance of GFM-VSC under a practical grid fault scenario, the time-domain simulation is carried out by considering the system configuration given by Fig. 20. The GFM-VSC is connected to the power grid through two paralleled transmission lines Z_{g1} (0.05 p.u.) and Z_{g2} (0.1 p.u.). Then, a three-phase to ground fault is applied to Z_{g2} with fault impedance Z_{gnd} (0.05 p.u.). After 200 ms, the fault is cleared by opening circuit breakers S3 and

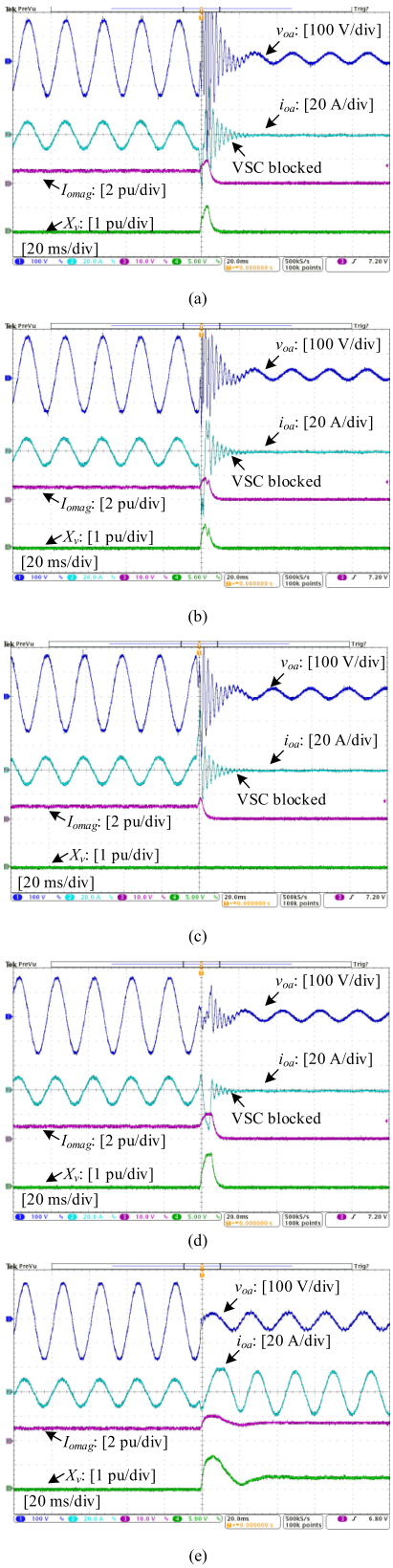

Fig. 19. Experimental results of GFM-VSC during grid faults (V_g drops to 0.2 p.u.) (a) No LPFs, unstable. (b) With $G_{\mathrm{LPF}R}$ only and $\omega_{\mathrm{LPF}R} = 2\pi{\cdot}10$ (rad/s), unstable. (c) With $G_{\mathrm{LPF}i}$ only and $\omega_{\mathrm{LPF}i} = 2\pi{\cdot}10$ (rad/s), unstable. (d) With $G_{\mathrm{LPF}X}$ only and $\omega_{\mathrm{LPF}X} = 2\pi{\cdot}50$ (rad/s), unstable. (e) With $G_{\mathrm{LPF}X}$ only and $\omega_{\mathrm{LPF}X} = 2\pi{\cdot}10$ (rad/s), stable.

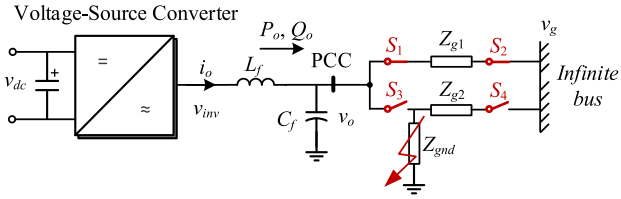

Fig. 20. Simulation setup of GFM-VSC with $Z_{g1} = 0.05$ p.u., $Z_{g2} = 0.1$ p.u., and $Z_{gnd} = 0.05$ p.u.

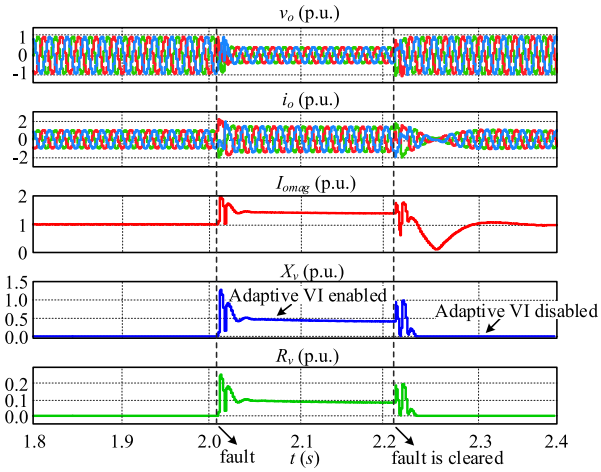

Fig. 21. Simulation results of GFM-VSC subjecting a three-phase to ground fault with $Z_{g1} = 0.05$ p.u., $Z_{g2} = 0.1$ p.u., and $Z_{gnd} = 0.05$ p.u.

S4. With this configuration, both grid voltage and equivalent grid impedance will change at the instant of grid fault as well as fault recovery.

Fig. 21 shows the simulation result of GFM-VSC with $G_{\mathrm{LPF}X}$ only and $\omega_{\mathrm{LPF}X} = 2\pi{\cdot}10$ (rad/s). It can be seen that the output voltage and current of GFM-VSC experience some oscillations at the instant of grid fault and fault recovery, due to the abrupt change of grid voltage and equivalent grid impedance. Nevertheless, the adaptive VI is still correctly activated to limit the steady-state fault current to 1.5 p.u. Moreover, it can be seen that the adaptive VI is automatically disabled after the fault clearance, and GFM-VSC is naturally switched back to the normal operation. The simulation results show that GFM-VSC with the designed adaptive VI also works well under a practical grid fault scenario.

VI. Conclusion

This article discusses the small-signal modeling and parameters tuning of GFM-VSCs with adaptive VI control. The major findings of this article are summarized as follows.

1) The frequency coupling dynamics of GFM-VSC is yielded due to the adaptive VI control that couples the current magnitude dynamics and the VI dynamics. This frequency coupling dynamics can be depicted by the FCIVI loop, which is crucial to the system stability.
2) Different from $G_{\mathrm{LPF}R}$ and $G_{\mathrm{LPF}i}$ that has limited or even adverse impact on system stability, $G_{\mathrm{LPF}X}$

contributes to stabilizing the system. Hence, only $G_{\mathrm{LPF}X}$ is recommended for implementing the adaptive VI. A systematic tuning of $\omega_{\mathrm{LPF}X}$ of $G_{\mathrm{LPF}X}$ is proposed in the article to stabilize the FCIVI loop and the adaptive VI loop.

3) The adaptive VI control, when activated, would lower the loop gain of the APC loop, which does not jeopardize its small-signal stability. Therefore, parameters tuning of the APC loop can still follow the guideline that considering the steady-state operation of GFM-VSC only.

All the findings are elaborated theoretically and confirmed by simulation and experimental tests.

APPENDIX A

The circuit dynamics of GFM-VSC can be expressed as

$$\begin{bmatrix} v^s_{\mathrm{inv}d} \\ v^s_{\mathrm{inv}q} \end{bmatrix} - \begin{bmatrix} v^s_{od} \\ v^s_{oq} \end{bmatrix} = \underbrace{\begin{bmatrix} sL_f & -\omega_0 L_f \\ \omega_0 L_f & sL_f \end{bmatrix}}_{\mathbf{Z}_{Lf}} \begin{bmatrix} i^s_{od} \\ i^s_{oq} \end{bmatrix}. \tag{A.1}$$

Considering the impact of the delay term, (45) can be rewritten as

$$\begin{aligned} \begin{bmatrix} \hat{v}^s_{\mathrm{inv}d} \\ \hat{v}^s_{\mathrm{inv}q} \end{bmatrix} = & -G_d \mathbf{Z}_{\mathbf{v\_tot dq}} \begin{bmatrix} \hat{i}^s_{od} \\ \hat{i}^s_{oq} \end{bmatrix} \\ & + \left(G_d \mathbf{Z}_{\mathbf{v\_tot dq}} \begin{bmatrix} -I^s_{oq0} \\ I^s_{od0} \end{bmatrix} + \begin{bmatrix} -V^s_{\mathrm{inv}q0} \\ V^s_{\mathrm{inv}d0} \end{bmatrix} \right) \hat{\delta}. \end{aligned} \tag{A.2}$$

Substituting (A.2) into (A.1), which yields

$$\begin{aligned} -\begin{bmatrix} \hat{v}^s_{od} \\ \hat{v}^s_{oq} \end{bmatrix} = & \underbrace{\left(\mathbf{Z}_{Lf} + G_d \mathbf{Z}_{\mathbf{v\_tot dq}}\right)}_{\mathbf{Z}_{\mathrm{con}}} \begin{bmatrix} \hat{i}^s_{od} \\ \hat{i}^s_{oq} \end{bmatrix} \\ & + \underbrace{\left(G_d \mathbf{Z}_{\mathbf{v\_tot dq}} \begin{bmatrix} I_{oqs} & 0 \\ 0 & -I_{ods} \end{bmatrix} + \begin{bmatrix} V_{\mathrm{inv}qs} & 0 \\ 0 & -V_{\mathrm{inv}ds} \end{bmatrix} \right)}_{\mathbf{M}} \begin{bmatrix} \hat{\delta} \\ \hat{\delta} \end{bmatrix}. \end{aligned} \tag{A.3}$$

It is known from Fig. 14 that $\hat{\delta}$ can be expressed as

$$\hat{\delta} = -\frac{1}{s} K_{\mathrm{APC}} G_{\mathrm{LPF}p} \hat{p}_o. \tag{A.4}$$

Substituting (A.4) and (51) into (A.3), the output impedance matrix of GFM-VSC in *dq* frame can be calculated as

$$\begin{bmatrix} \hat{v}^s_{od} \\ \hat{v}^s_{oq} \end{bmatrix} = \underbrace{\left(\mathbf{I} + \mathbf{M}\mathbf{I}_{\mathbf{odq}}\right)^{-1} \left(\mathbf{Z}_{\mathrm{con}} + \mathbf{M}\mathbf{V}_{\mathbf{odq}}\right)}_{\mathbf{Z}_{\mathrm{GFM}\mathbf{dq}}} \begin{bmatrix} \hat{i}^s_{od} \\ \hat{i}^s_{oq} \end{bmatrix} \tag{A.5}$$

where

$$\mathbf{V}_{\mathbf{odq}} = \frac{3}{2} \begin{bmatrix} -\frac{G_{\mathrm{LPF}p} K_{\mathrm{APC}}}{s} V_{ods} & -\frac{G_{\mathrm{LPF}p} K_{\mathrm{APC}}}{s} V_{oqs} \\ -\frac{G_{\mathrm{LPF}p} K_{\mathrm{APC}}}{s} V_{ods} & -\frac{G_{\mathrm{LPF}p} K_{\mathrm{APC}}}{s} V_{oqs} \end{bmatrix} \tag{A.6}$$

$$\mathbf{I}_{\mathbf{odq}} = \frac{3}{2} \begin{bmatrix} -\frac{G_{\mathrm{LPF}p} K_{\mathrm{APC}}}{s} I_{ods} & -\frac{G_{\mathrm{LPF}p} K_{\mathrm{APC}}}{s} I_{oqs} \\ -\frac{G_{\mathrm{LPF}p} K_{\mathrm{APC}}}{s} I_{ods} & -\frac{G_{\mathrm{LPF}p} K_{\mathrm{APC}}}{s} I_{oqs} \end{bmatrix}. \tag{A.7}$$

The *dq*-framed impedance matrix given in (A.5) can be further transformed to $\alpha\beta$ frame with complex-vector representation [31]–[34], i.e.,

$$\begin{bmatrix} \hat{v}_{o\alpha\beta}(s) \\ \hat{v}^*_{o\alpha\beta}(s - 2j\omega_0) \end{bmatrix} = \mathbf{Z}_{\mathrm{GFM}\alpha\beta}(s) \begin{bmatrix} \hat{i}_{o\alpha\beta}(s) \\ \hat{i}^*_{o\alpha\beta}(s - 2j\omega_0) \end{bmatrix} \tag{A.8}$$

where

$$\mathbf{Z}_{\mathrm{GFM}\alpha\beta}(s) = \mathbf{Z}_{\mathrm{GFM}\mathbf{dqc}}(s - j\omega_0) \tag{A.9}$$

$$\mathbf{Z}_{\mathrm{GFM}\mathbf{dqc}}(s) = \mathbf{T}\mathbf{Z}_{\mathrm{GFM}\mathbf{dq}}(s)\,\mathbf{T}^{-1} \tag{A.10}$$

where matrix $\boldsymbol{T}$ is given by (16).

REFERENCES

[1] J. Matevosyan *et al.*, "GFM inverters," *IEEE Power Energy Mag.*, vol. 17, no. 6, pp. 89–98, Nov./Dec. 2019.

[2] L. Zhang, L. Harnefors, and H.-P. Nee, "Power-synchronization control of grid-connected voltage-source converters," *IEEE Trans. Power Syst.*, vol. 25, no. 2, pp. 809–820, May 2010.

[3] H. Wu and X. Wang, "Design-oriented transient stability analysis of grid-connected converters with power synchronization control," *IEEE Trans. Ind. Electron.*, vol. 66, no. 8, pp. 6473–6482, Aug. 2019.

[4] D. Pan, X. Wang, F. Liu, and R. Shi, "Transient stability of voltage source converters with grid-forming control: A design-oriented study," *IEEE J. Emerg. Sel. Topics Power Electron.*, vol. 8, no. 2, pp. 1019–1033, Jun. 2020.

[5] H. Hooshyar and M. E. Baran, "Fault analysis on distribution feeders with high penetration of PV systems," *IEEE Trans. Power Syst.*, vol. 28, no. 3, pp. 2890–2896, Aug. 2013.

[6] M. G. Taul, X. Wang, P. Davari, and F. Blaabjerg, "Current limiting control with enhanced dynamics of grid-forming converters during fault conditions," *IEEE J. Emerg. Sel. Topics Power Electron.*, vol. 8, no. 2, pp. 1062–1073, Jun. 2019.

[7] X. Wang, M. G. Taul, H. Wu, Y. Liao, F. Blaabjerg, and L. Harnefors, "Grid-synchronization stability of converter-based resources—An overview," *IEEE Open J. Ind. Appl.*, vol. 1, pp. 115–134, Aug. 2020.

[8] R. Rosso, X. Wang, M. Liserre, X. Lu, and S. Engelken, "Grid-forming converters: Control approaches, grid-synchronization, and future trends—A review," *IEEE Open J. Ind. Appl.*, vol. 2, pp. 93–109, Apr. 2021.

[9] N. Bottrell and T. C. Green, "Comparison of current-limiting strategies during fault ride-through of inverters to prevent latch-up and wind up," *IEEE Trans. Power Electron.*, vol. 29, no. 7, pp. 3786–3797, Jul. 2014.

[10] L. Huang, H. Xin, Z. Wang, L. Zhang, K. Wu, and J. Hu, "Transient stability analysis and control design of droop-controlled voltage source converters considering current limitation," *IEEE Trans. Smart Grid*, vol. 10, no. 1, pp. 578–591, Jan. 2019.

[11] H. Wu and X. Wang, "Design-oriented transient stability analysis of PLL-synchronized voltage-source converters," *IEEE Trans. Power Electron.*, vol. 35, no. 4, pp. 3573–3589, Apr. 2020.

[12] R. Rosso, S. Engelken, and M. Liserre, "On the implementation of a FRT strategy for grid-forming (GFM) converters under symmetrical and asymmetrical grid faults," *IEEE Trans. Ind. Appl.*, vol. 57, no. 5, pp. 4385–4397, Sep./Oct. 2021.

[13] A. Johnson and P. Simango, "RfG—Fast fault current injection," Nat. Grid ESO, Apr. 2017.

[14] "High penetration of power electronic interfaced power sources and the potential contribution of grid forming converters," ENTSO-E Tech. Rep., 2020.

[15] "Draft grid code-grid forming converter specification," Nat. Grid ESO, Sep. 2020.

[16] J. Chen, F. Prystupczuk, and T. O'Donnell, "Use of voltage limits for current limitations in grid-forming converters," *CSEE J. Power Energy Syst.*, vol. 6, no. 2, pp. 259–269, Jun. 2020.

[17] X. Lu, J. Wang, J. M. Guerrero, and D. Zhao, "Virtual-impedance-based fault current limiters for inverter dominated AC microgrids," *IEEE Trans. Smart Grid*, vol. 9, no. 3, pp. 1599–1612, May 2018.

[18] F. Welck, D. Duckwitz, and C. Gloeckler, "Influence of virtual impedance on short circuit performance of virtual synchronous machines in the 9-bus system," in *Proc. Conf. Sustain. Energy Supply Energy Storage Syst.*, Sep. 2017, pp. 1–7.

[19] T. Qoria, F. Gruson, F. Colas, G. Denis, T. Prevost, and X. Guillaud, "Critical clearing time determination and enhancement of grid-forming converters embedding virtual impedance as current limitation algorithm," *IEEE J. Emerg. Sel. Topics Power Electron.*, vol. 8, no. 2, pp. 1050–1061, Jun. 2020.
[20] T. Qoria, F. Gruson, F. Colas, X. Kestelyn, and X. Guillaud, "Current limiting algorithms and transient stability analysis of grid-forming VSCs," *Elect. Power Syst. Res.*, vol. 189, Dec. 2020, Art. no. 106726.
[21] A. D. Paquette and D. M. Divan, "Virtual impedance current limiting for inverters in microgrids with synchronous generators," *IEEE Trans. Ind. Appl.*, vol. 51, no. 2, pp. 1630–1638, Mar./Apr. 2015.
[22] H. Wu *et al.*, "Small-signal modeling and parameters design for virtual synchronous generators," *IEEE Trans. Ind. Electron.*, vol. 63, no. 7, pp. 4292–4303, Jul. 2016.
[23] L. Zhang, "Modeling and control of VSC-HVDC links connected to weak AC systems," Ph.D. dissertation, Dept. Elect. Eng., KTH, Stockholm, Sweden, 2011.
[24] L. Harnefors, M. Hinkkanen, U. Riaz, F. M. M. Rahman, and L. Zhang, "Robust analytic design of power-synchronization control," *IEEE Trans. Ind. Electron.*, vol. 66, no. 8, pp. 5810–5819, Aug. 2019.
[25] W. Du *et al.*, "A comparative study of two widely used grid forming droop controls on microgrid small-signal stability," *IEEE J. Emerg. Sel. Topics Power Electron.*, vol. 8, no. 2, pp. 963–975, Jun. 2020.
[26] S. Wang, Z. Liu, J. Liu, D. Boroyevich, and R. Burgos, "Small-signal modeling and stability prediction of parallel droop-controlled inverters based on terminal characteristics of individual inverters," *IEEE Trans. Power Electron.*, vol. 35, no. 1, pp. 1045–1063, Jan. 2020.
[27] G. Li *et al.*, "Analysis and mitigation of sub-synchronous resonance in series-compensated grid-connected system controlled by virtual synchronous generator," *IEEE Trans. Power Electron.*, vol. 35, no. 10, pp. 11096–11107, Oct. 2020.
[28] T. Liu and X. Wang, "Transient stability of single-loop voltage magnitude controlled grid-forming converters," *IEEE Trans. Power Electron.*, vol. 36, no. 6, pp. 6158–6162, Jun. 2021.
[29] H. Wu and X. Wang, "Passivity-based dual-loop vector voltage and current control for grid-forming VSCs," *IEEE Trans. Power Electron.*, vol. 36, no. 8, pp. 8647–8652, Aug. 2021.
[30] G. F. Franklin, J. D. Powell, and A. Emami-Naeini, *Feedback Control of Dynamic Systems*. London, U.K.: Pearson Educ., 2015.
[31] L. Harnefors, X. Wang, S. Chou, M. Bongiorno, M. Hinkkanen, and M. Routimo, "Asymmetric complex-vector models with application to VSC–grid interaction," *IEEE J. Emerg. Sel. Topics Power Electron.*, vol. 8, no. 2, pp. 1911–1921, Jun. 2020.
[32] X. Wang, L. Harnefors, and F. Blaabjerg, "A unified impedance model of grid-connected voltage-source converters," *IEEE Trans. Power Electron.*, vol. 33, no. 2, pp. 1775–1787, Feb. 2018.
[33] C. Zhang, M. Molinas, A. Rygg, J. Lyu, and X. Cai, "Harmonic transfer-function-based impedance modeling of a three-phase VSC for asymmetric AC grid stability analysis," *IEEE Trans. Power Electron.*, vol. 34, no. 12, pp. 12552–12566, Dec. 2019.
[34] S. Shah and L. Parsa, "Impedance modeling of three-phase voltage source converters in DQ, sequence, and phasor domains," *IEEE Trans. Energy Convers.*, vol. 32, no. 3, pp. 1139–1150, Sep. 2017.
[35] Y. Liao, X. Wang, F. Liu, K. Xin, and Y. Liu, "Sub-synchronous control interaction in grid-forming VSCs with droop control," in *Proc. 4th IEEE Workshop Electron. Grid*, May 2019, pp. 1–6.
[36] L. Harnefors, F. M. M. Rahman, M. Hinkkanen, and M. Routimo, "Reference-feedforward power-synchronization control," *IEEE Trans. Power Electron.*, vol. 35, no. 9, pp. 8878–8881, Sep. 2020.
[37] *Requirements for the Connection of Micro Generators in Parallel With Public Low-Voltage Distribution Networks*, EN 50438, 2008.

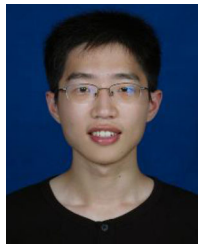

Heng Wu (Member, IEEE) received the B.S. and M.S. degrees in electrical engineering from the Nanjing University of Aeronautics and Astronautics, Nanjing, China, in 2012 and 2015, respectively, and the Ph.D. degree in electrical engineering from Aalborg University, Aalborg, Denmark, in 2020.

He is currently an Assistant Professor with AAU Energy, Aalborg University. From 2015 to 2017, he was an Electrical Engineer with NR Electric Co., Ltd, Nanjing, China. He was a Guest Researcher with Ørsted Wind Power, Fredericia, Denmark, in 2018, and Bundeswehr University, Munich, Germany, in 2019. He was a Postdoctoral Researcher with Aalborg University, from 2020 to 2021. His research interests include the modeling and stability analysis of the power electronic based power systems.

Dr. Wu is the Co-Chair of IEEE Task Force on Frequency-Domain Modeling and Dynamic Analysis of HVdc and FACTS, the member of Cigre working group B4.85, and the Steering Committee Member of Cigre Next Generation Network, Denmark. He has been identified as world's top 2% scientist by Stanford University since 2019. He was the recipient of the 2019 Outstanding Reviewer Award of the IEEE TRANSACTIONS ON POWER ELECTRONICS.

Xiongfei Wang (Senior Member, IEEE) received the B.S. degree from Yanshan University, Qinhuangdao, China, in 2006, the M.S. degree from the Harbin Institute of Technology, Harbin, China, in 2008, both in electrical engineering, and the Ph.D. degree in energy technology from Aalborg University, Aalborg, Denmark, in 2013.

Since 2009, he has been with the Department of Energy Technology, Aalborg University, where he became an Assistant Professor in 2014, an Associate Professor in 2016, a Professor and Leader of Electronic Power Grid Research Group in 2018. He has also been a Visiting Professor with the KTH Royal Institute of Technology, Stockholm, Sweden, since 2020. His research interests include modeling and control of power electronic converters and systems, stability and power quality of power-electronics-dominated power systems, and high-power converters.

Prof. Wang serves as a Member-at-Large of Administrative Committee for the IEEE Power Electronics Society (PELS) in 2020–2022, a Co-Editor-in-Chief for the IEEE TRANSACTIONS ON POWER ELECTRONICS LETTERS, and as an Associate Editor for the IEEE JOURNAL OF EMERGING AND SELECTED TOPICS IN POWER ELECTRONICS (JESTPE). He was selected into Aalborg University Strategic Talent Management Program in 2016. He was the recipient of six Prize Paper Awards in the IEEE Transactions and conferences, the 2018 Richard M. Bass Outstanding Young Power Electronics Engineer Award, the 2019 IEEE PELS Sustainable Energy Systems Technical Achievement Award, the 2020 IEEE Power and Energy Society Prize Paper Award, the 2020 JESTPE Star Associate Editor Award, and the Highly Cited Researcher in the Web of Science in 2019–2021.